LEVEL

UILU-ENG-80-2553

THE STUDY AND IDENTIFICATION OF RESIDUAL DONOR SPECIES IN

HIGH PURITY SEMICONDUCTORS

T. S. Low
and
G. E. Stillman
Department of Electrical Engineering
University of Illinois
Urbana, IL   61801

November 1980

Final Report for N00173-79-C-0184
for period 4 June 1979 to 31 July 1980

Distribution Unlimited.

Prepared for

DISTRIBUTION STATEMENT A

Approved for public release
Distribution Unlimited

AD A092542

DTIC
ELECTE
DEC 2 9 1980
S
C

DDC FILE COPY

80 12 24 049

REPORT DOCUMENTATION PAGE	READ INSTRUCTIONS BEFORE COMPLETING FORM

1. REPORT NUMBER	2. GOVT ACCESSION NO.	3. RECIPIENT'S CATALOG NUMBER
	AD A092542	

4. TITLE (and Subtitle)	5. TYPE OF REPORT & PERIOD COVERED
THE STUDY AND IDENTIFICATION OF RESIDUAL DONOR SPECIES IN HIGH PURITY SEMICONDUCTORS.	Final Report. 4 June 1979 — 31 July 1980
	6. PERFORMING ORG. REPORT NUMBER
	UILU-ENG-80-2553

7. AUTHOR(s)	8. CONTRACT OR GRANT NUMBER(s)
T. S. Low and G. E. Stillman	N00173-79-C-0184

9. PERFORMING ORGANIZATION NAME AND ADDRESS	10. PROGRAM ELEMENT, PROJECT, TASK AREA & WORK UNIT NUMBERS
Department of Electrical Engineering University of Illinois at Urbana-Champaign Urbana, Illinois 61801	

11. CONTROLLING OFFICE NAME AND ADDRESS	12. REPORT DATE
Naval Research Laboratory Mr. Howard Lessoff, Code 6820, Scientific Monitor Washington, D.C. 20375	November 1980
	13. NUMBER OF PAGES
	63

14. MONITORING AGENCY NAME & ADDRESS(if different from Controlling Office)	15. SECURITY CLASS. (of this report)
	15a. DECLASSIFICATION/DOWNGRADING SCHEDULE

16. DISTRIBUTION STATEMENT (of this Report)

Distribution Unlimited

DISTRIBUTION STATEMENT A

Approved for public release;
Distribution Unlimited

17. DISTRIBUTION STATEMENT (of the abstract entered in Block 20, if different from Report)

19. KEY WORDS (Continue on reverse side if necessary and identify by block number)

GaAs; Shallow impurities; Shallow donors; Fourier transform; Residual impurities; Residual donors; High purity semiconductors; Phase correction.

20. ABSTRACT (Continue on reverse side if necessary and identify by block number)

A far infrared Fourier transform spectroscope has been constructed which uses photothermal ionization to probe the energy level structure of shallow impurities, enabling identification and measurement of relative concentrations of residual impurity species in high purity semiconductors. Spectra from samples grown by MO-CVD, MBE, LPE, and both hydride and chloride VPE are shown and analyzed. Some mathematical details about the Fourier transform are considered and a computer investigation of spectral line shape distortion by the transform is described.

DD FORM 1473 EDITION OF 1 NOV 65 IS OBSOLETE

UILU-ENG-80-2553

THE STUDY AND IDENTIFICATION OF RESIDUAL DONOR SPECIES IN

HIGH PURITY SEMICONDUCTORS

T. S. Low
and
G. E. Stillman
Department of Electrical Engineering
University of Illinois
Urbana, IL   61801

November 1980

Distribution Unlimited.

Prepared for

The views and conclusions contained in this document are those of
the authors and should not be interpreted as necessarily representing
the official policies, either expressed or implied, of the Naval
Research Laboratory or the U. S. Government.

Photothermal ionization spectroscopy is an extremely sensitive technique for the detection and identification of small concentrations of impurities in semiconductors. It has been used extensively in Si, Ge and GaAs. Identification of many of the shallow donors in GaAs with their corresponding spectral peaks has been accomplished. This provides a useful tool for the characterization of high purity semiconductors giving the crystal grower information about type and relative concentration of residual impurities in high purity material. We describe here an apparatus which has been constructed to perform such measurements and the theory of its operation. Spectra of samples from a number of university, industrial and government laboratories have been measured. These samples have been grown by a wide variety of growth techniques including MO-CVD, MBE, LPE and both hydride and chloride VPE. The spectra of these samples are shown in the figures and analyzed in detail in the text. Finally, a computer investigation of the effects of the Fourier transform of the data on spectral line shape is described. This is of interest because the spectral line shapes may be useful as a tool to study impurity-impurity interactions. It is thus imperative that the Fourier transform of the data reflect the true photothermal ionization line shape.

TABLE OF CONTENTS

LIST OF FIGURES

BASIC THEORY

For an isolated impurity, a simple hydrogenic model can be used to estimate the impurity energy levels. A donor atom, relative to the host atom it replaces, has one extra valence electron and one extra positive charge on its ion core. To the extent that electrons in the conduction band behave as free electrons, this is analogous to a hydrogen atom in a vacuum. Using the dielectric constant and effective mass appropriate for the semiconductor (instead of for the vacuum) a model Hamiltonian for the donor electron can be written:

$$(1) \qquad H = \frac{-\hbar^2}{2m^*} \nabla^2 - \frac{e^2}{\varepsilon_o r}$$

Except for the replacement of m by m^* and e^2 by $\frac{e^2}{\varepsilon_o}$, this is the familiar Hamiltonian of the hydrogen atom. The replacements simply rescale the energy and distance scales of the hydrogenic solutions giving the energy spectrum and Bohr radius as:

$$(2) \qquad E_n = m^* e^4 / 2\varepsilon_o^2 \hbar^2 n^2 = [(m^*/m)/\varepsilon_o^2 n^2] \ 13.6 \ eV$$

$$(3) \qquad a_B = (\hbar^2/m^* e^2)\varepsilon_o = [\varepsilon_o/(m^*/m)] \ .529 \ Å$$

where (m^*/m) is the effective mass ratio and ε_o is the static dielectric constant of the semiconductor.

The ionization energies and Bohr radii calculated from (2) and (3) for donors in several semiconductors are given in Table I. This picture for electrons can be more rigorously derived by approximations to one electron band theory[1] and can be extended to the cases of anisotropic effective masses and multiple conduction band minima. When this is done, the analogue of (1) becomes intractable analytically, but the variationally derived energies

1

TABLE I

Ionization Energies and Bohr Radius
Calculated from the Simple Hydrogenic Model

Semiconductor	$\frac{m^*}{m}$	ϵ_0	E_D (meV)	a_B (Å)	$\frac{a_B}{a_0}$	a_0 (Å)
Si	0.4^a	11.40	41.7	15	2.8	5.43072
Ge	0.2^a	15.36	11.5	41	7.2	5.65754
GaAs	0.0665	12.5	5.77	99	17.6	5.65315
InSb	0.013	16	.689	650	100	6.47877

a. The effective masses used for Si and Ge are average scalar effective masses. For more accurate values of E_D and a_B the nonisotropic effective masses and revised effective mass theory must be used.
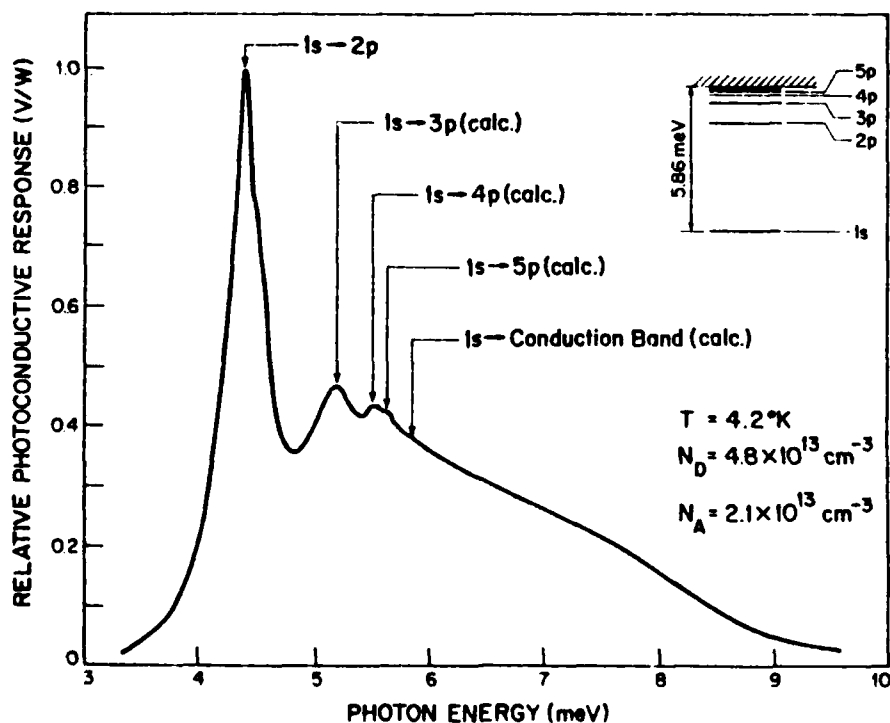

Figure 1. Typical photothermal ionization spectrum for zero magnetic field.

agree well with those deduced from absorption or photothermal ionization measurements, at least for the excited states.

Another correction to the hydrogenic model is due to the fact that the conduction band is not precisely parabolic about its minima. The non-parabolic corrections to the donor energy levels can be estimated from Kanes $\vec{k} \cdot \vec{p}$ [2] calculation of E(k) for small k and are less than .005 E_1 in GaAs. The agreement between transition energies predicted from the simple hydrogenic theory and those observed in a high purity GaAs sample's photoconductivity spectrum can be seen in Fig.1.

It is important to note that the hydrogenic model above predicts identical ionization energies for different donor species. This is not observed experimentally. The reason for this is that for distances less than a few lattice constants the potential felt by the donor electron is no longer the simple screened coulombic potential in (1) but rather is determined by the species dependent details of the electronic structure of the donor ion core and the local distortion of the lattice around it. To our knowledge, no satisfactory calculations of this effect have been made. In spite of this interesting complication, for small binding energies the donor wavefunctions are quite extended and their overlap with the region where the potential deviates from coulombic is small. The result is that the difference between the predicted hydrogenic ground state energy and the measured value (termed the central cell correction or chemical shift) is small. In GaAs the donor states are sufficiently extended that the central cell corrections are only a few percent of the donor ground state energy. The impurity species dependence of the central cell corrections is of great interest since it has allowed the tentative identification of many of the donors in GaAs.[3] Measured ground state central cell corrections for various donor species in GaAs are given in Table II.

3

TABLE II   Central Cell Corrections to the Parabolic Band $Ry^*(= 46.10 \text{ cm}^{-1})$, for Four Residual Donors in High Purity GaAs

Donor	Central Cell Correction	Ionization Energy[a,b]
1	.064 meV (.52 cm^{-1})	5.800 meV (46.79 cm^{-1})
2	.081 meV (.65 cm^{-1})	5.817 meV (46.92 cm^{-1})
3	.117 meV (.94 cm^{-1})	5.854 meV (47.22 cm^{-1})
4	.200 meV (1.61 cm^{-1})	5.937 meV (47.89 cm^{-1})

a.   The ionization energies include the deepening of the 1s state due to both central cell shifts and conduction band nonparabolicity.

b.   The magnitudes of the ionization energies are accurate within about $\pm 0.15 \text{ cm}^{-1}$, while the differences between the energies are known to about $\pm 0.01 \text{ cm}^{-1}$.

EXPERIMENTAL METHOD

A means by which the energy level spectra and the associated central cell corrections may be measured in high purity semiconductors is photothermal ionization spectroscopy. This an extremely sensitive method for analysis of impurities in high purity semiconductors. Other methods, such as optical absorption and mass spectrometry, are inadequate to identify impurities at the extremely small concentrations present in high purity material.

The photothermal ionization technique is based on the fact that the extrinsic photoconductivity spectrum under certain conditions is a line spectrum which corresponds to the bound electron energy levels of the impurities. The technique's sensitivity is due to the fact that the magnitude of the photoresponse does not decrease with decreasing impurity concentration down to very low concentrations. This is a consequence of the voltage sensitivity of the extrinsic photoconductivity being proportional to $\Delta n/n$, where n is the total carrier concentration without illumination and Δn is the change in carrier concentration under illumination. Both n and Δn are proportional to the concentration of major and compensating impurities and so this dependence cancels out of the voltage sensitivity.[4] This feature of the method enables the detection and identification of impurity species even in the highest purity semiconductor material which can be grown.[5]

Photothermal ionization spectroscopy requires a tunable far infrared light source and some means for recording the sample's electrical conductivity. The sample temperature is chosen such that $kT << E_1$ and nearly all of the uncompensated donors are occupied by a ground state electron. When

5

the far infrared light source is turned on, if the photon energy $h\nu \geq E_1$, some of these electrons can be excited directly to the conduction band increasing the conductivity of the sample. (See Fig. 2(a).) In principle, it would be possible to measure ionization energies by measuring the threshold of such a process, but in practice the threshold is not sharp enough to permit this measurement.

Under certain conditions, however, the extrinsic photoconductivity is dominated by a multistep process called photothermal ionization and it is this process through which the impurity energy spectra are obtained. The mechanism for photothermal ionization can be understood by considering a donor electron in its ground state. This electron can make a transition to one of the donor's excited states by absorption of a far infrared photon of appropriate energy. The still bound electron can then be excited to the conduction band (by absorption of phonon(s)) where it can contribute to the samples conductivity. (See Fig. 2(b).) Suppose one is probing the 1s-2p transition. When the light source is tuned through $h\nu = (E_{2p} - E_{1s})$ there is a peak in the electrical conductivity which corresponds to a 1s-2p photon absorption followed by absorption of phonon(s) which excites the impurity electron into the conduction band. The sample temperature is chosen such that there are ample phonons energetic enough to carry an electron from the excited state of interest to the conduction band, and yet few phonons sufficiently energetic to excite electrons from the impurity ground state. In GaAs this limits the temperature to a range of about 1.5 to 6 Kelvins.[6]

When a GaAs sample containing shallow donor impurities is placed in a magnetic field, the three-fold degeneracy of the p states is lifted. These states are labeled in the same way as the corresponding states in the hydrogen atom ($np(m=0,\pm 1)$). When the magnetic field is increased from 0 to 7.5 kilogauss,
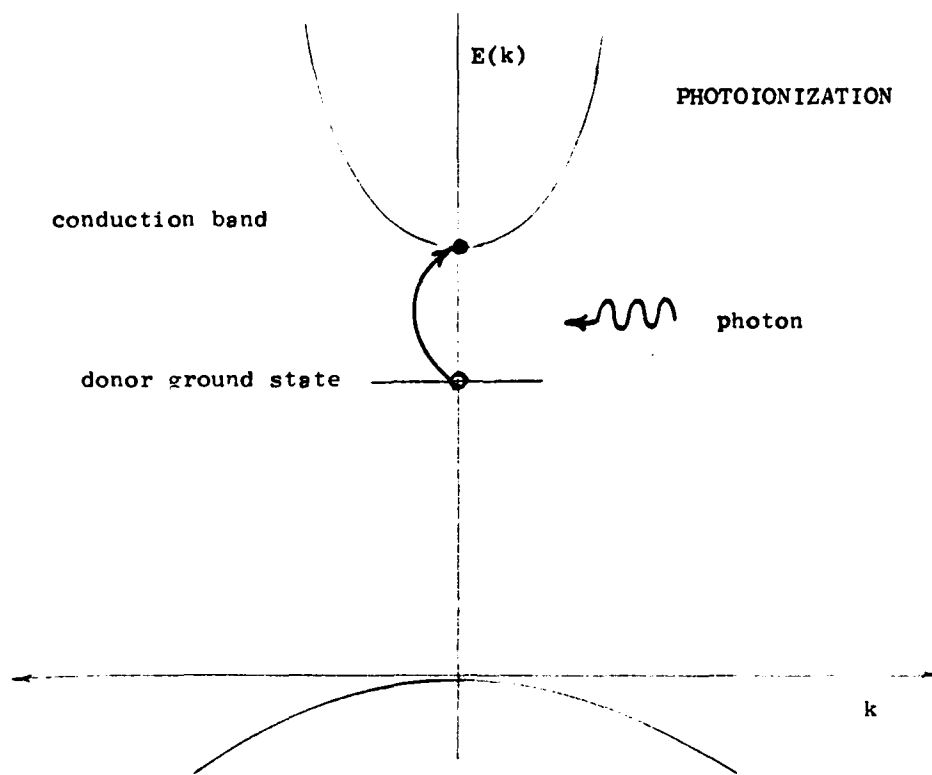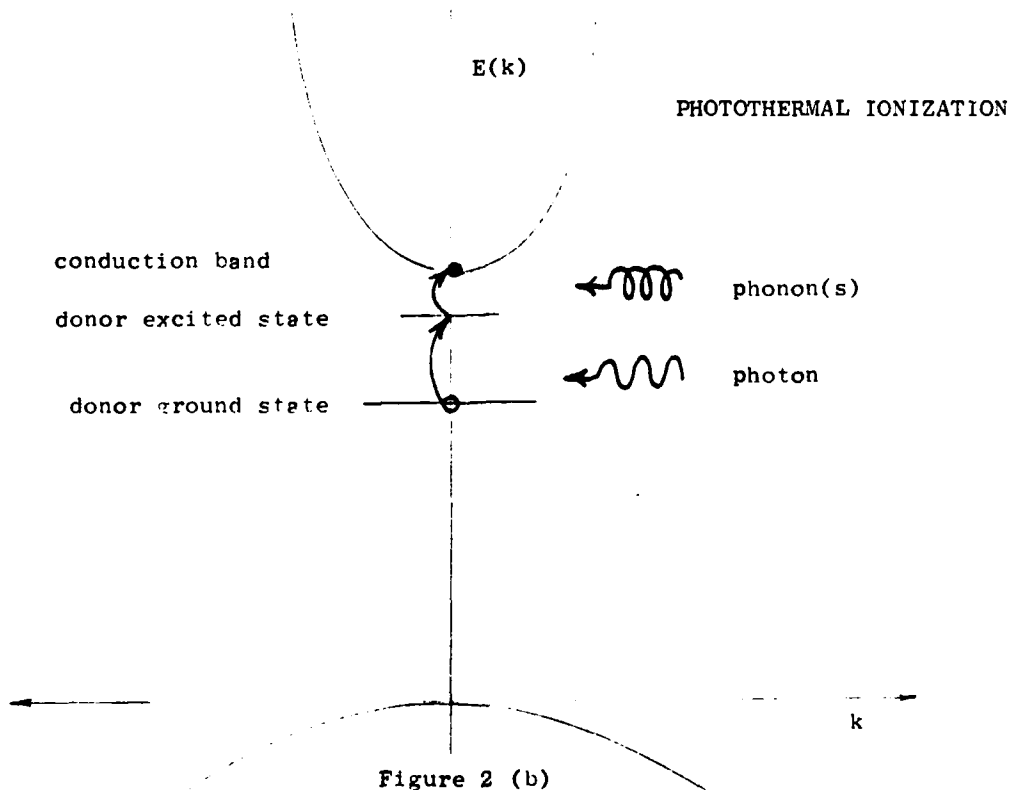
6

Figure 2. Microscopic picture of photoconductive processes.

the dominant 1s-2p peak seen in the zero field spectrum splits into three

peaks corresponding to 1s-2p (m=-1,0,+1) transitions. (See Figs. 3(a) and

(b).) A triplet also appears at higher energy which is attributed to the

1s-3p(m= -1, 0, + 1) transitions.

As the field is increased further, the lines in the photoconductivity

spectrum continue to separate and become narrower. (See Figs. 3(c) and (d).)

The width and shape of these lines are determined by Stark shifts of the

donor energy levels induced by the random distribution of electric fields

at the sites of donors in the crystal. These fields originate from the

spatial distribution of charged acceptors and ionized donors. D.M. Larsen

has predicted line shapes for the 1s-2p transitions on the basis of such a

model which agree well with line shapes observed in high purity GaAs samples.[7]

In very pure uncompensated samples when the field has reached 50 kilogauss,

the 1s-2p (m= -1) line width has shrunk from a zero field value of about

5 cm^{-1} to as little as 0.5 cm^{-1} and peaks corresponding to transitions to

other hydrogenic excited states are clearly resolved. Figure 4 shows a

high resolution spectrum of a high purity sample at 52.5 kilogauss. Notice

that both the 1s-2p (m= -1) and the 1s-2p (m=0) transitions have developed

a fine structure which was not apparent at zero field. This fine structure

is the result of the central cell shift of the donor ground state energy,

which is, in general, different for different impurity species. The energy

of the 2p state is almost totally unaffected by the central cell potential

since the p wavefunctions are zero at r=0. As a result, the 1s-2p transition

energy is impurity dependent primarily through the 1s central cell correction.

The 1s-2p (m=-1) transitions are of particular interest since they have

the largest amplitude and are the narrowest in .e 50 kilogauss spectrum.

At this high field, three conditions have conspired to facilitate impurity
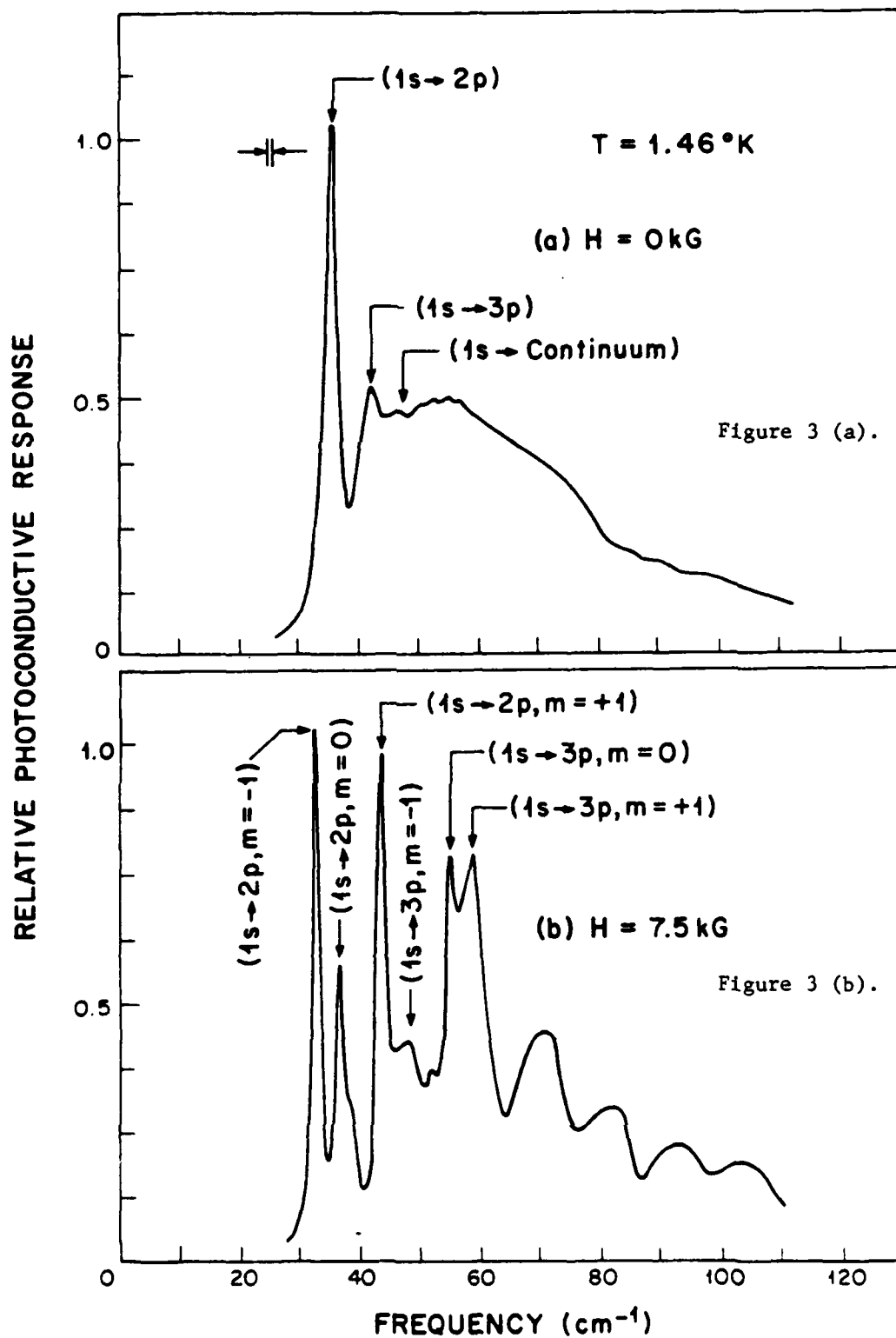
8

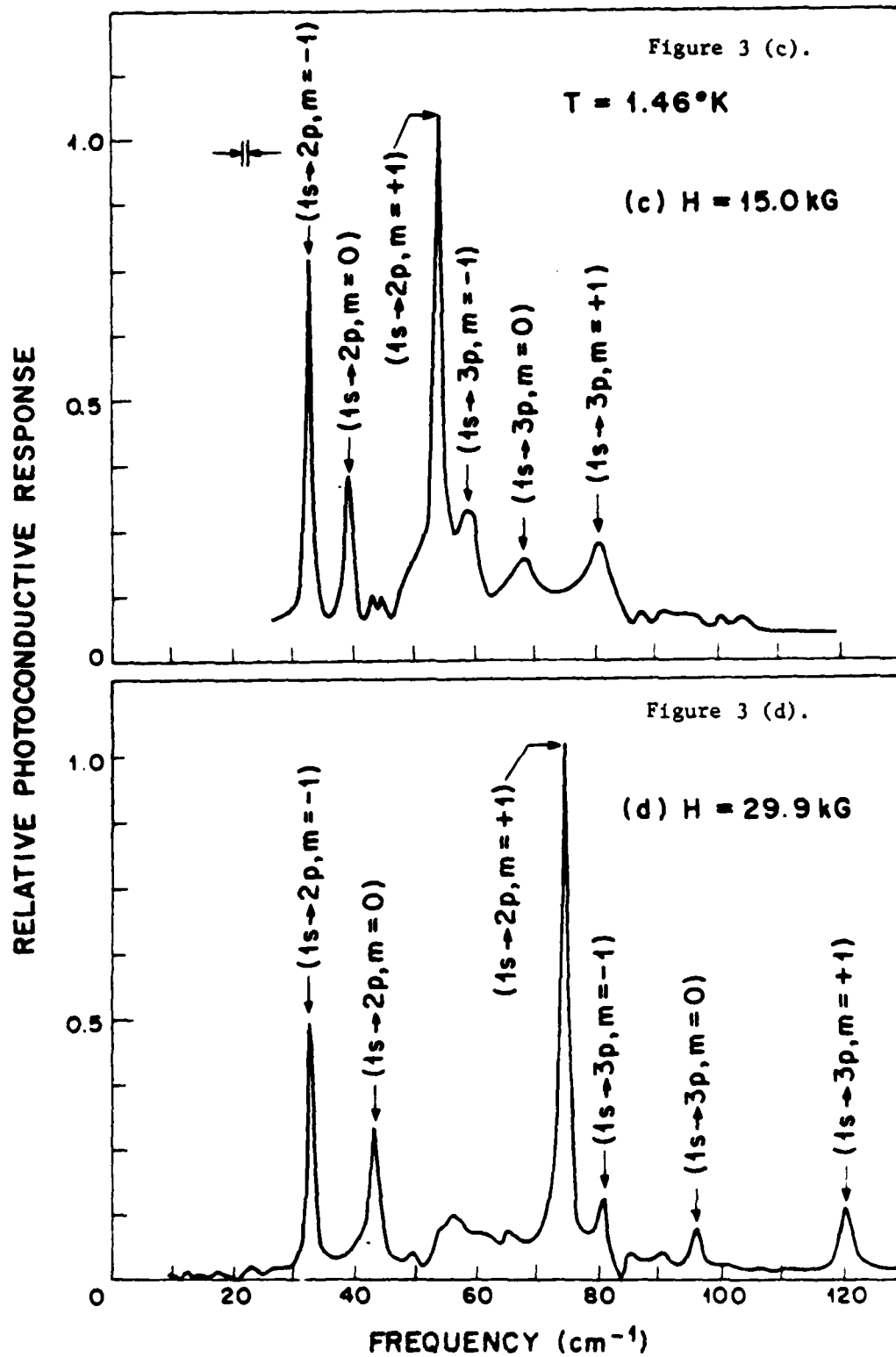Figure 3. Photothermal ionization spectra at several magnetic fields.

9

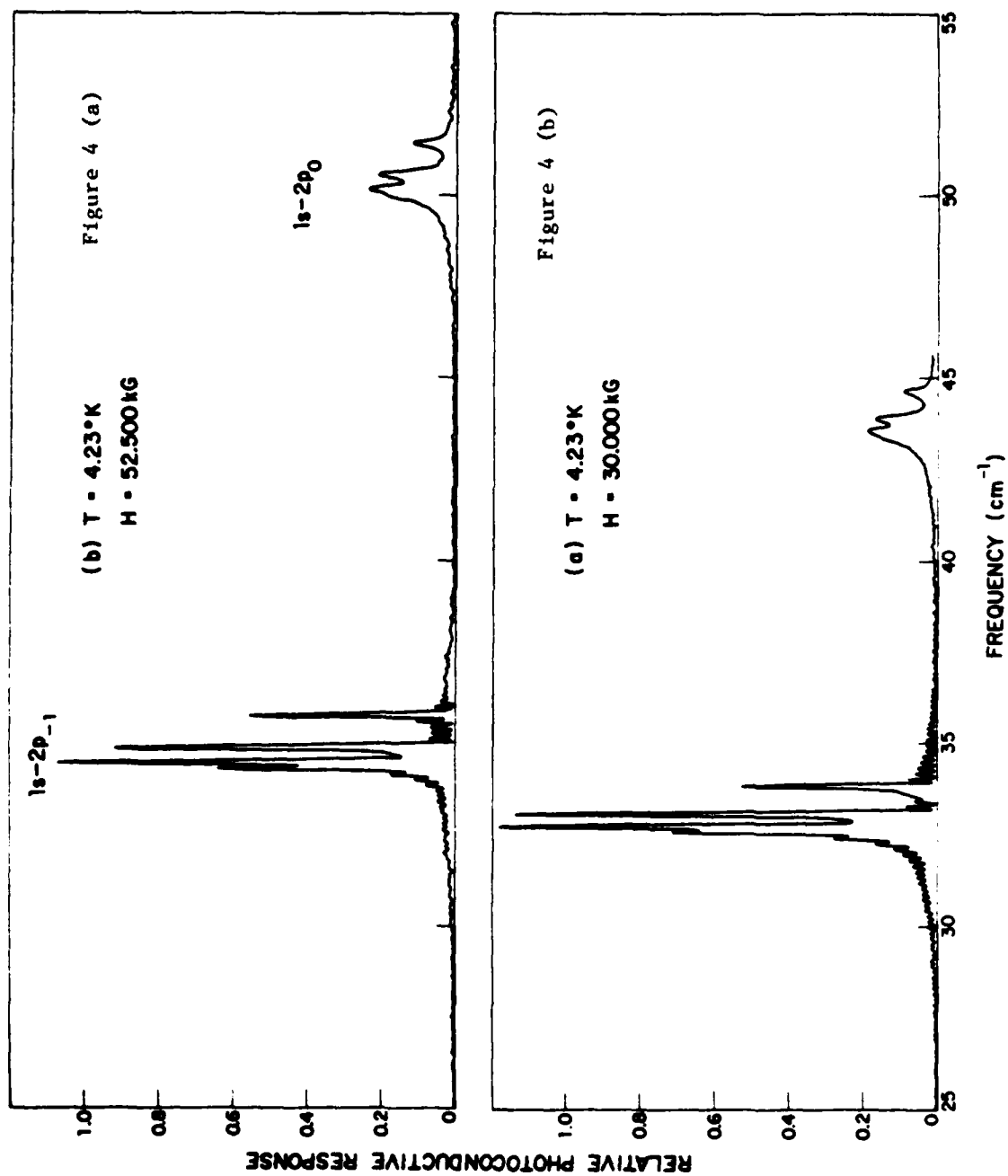Figure 3. Photothermal ionization spectra at several magnetic fields.

10

Figure 4. High resolution photothermal ionization spectra in GaAs.

identification using the 1s-2p (m=-1) transition. The 1s-2p (m=-1) lines

have been Zeeman split away in energy from the other broader 1s-2p lines.

The electric quadrupole moment of the 2p (m=-1) state has been reduced

nearly to zero and so the main contribution to Stark broadening of the

1s-2p (m=1) transition has been removed. Finally, the compression of the

1s wavefunction by the magnetic field has increased the overlap with the

central cell and so has increased the central cell shifts of the 1s state.

As a result in very high purity GaAs, it is possible to resolve peaks in this

transition corresponding to many different donor species. The relative

position of a peak within the 1s-2p (m=-1) envelope has been used as a

signature of a given donor species, and many of the donors in GaAs have

been tentatively identified in this way. The identifications due to C.M.

Wolfe, G.E. Stillman and D.M. Korn[3] are shown in Fig.5.

A block diagram of the apparatus used for the far infrared photo-

conductivity measurements appears in Fig.6(a). It consists of a spectrometer,

a cryostat, and the LSI-11 minicomputer based data acquisition system. The

cryostat includes a superconducting magnet which can expose the sample to a

0.1% uniform field of up to 67 kilogauss. Because the spectrometer, coupling

optics, and cryostat are sensitive to vibrations, they have been mounted on

an optical table which in turn rests on a large concrete pillar sunk in the

ground (separate from the building's floor vibrations).

The spectrometer (see Fig.6(b)) is a Beckman FS720 Michelson interferometer

which is used as a high resolution (± 0.06 cm^{-1}) tunable (5 cm^{-1} to 1000 cm^{-1})

far infrared light source for illuminating the semiconductor sample. Its

operation can be understood in the following way. The beamsplitter divides

the collimated light from the source into two beams. One beam travels a

fixed path length while the other travels a path length which is variable

by means of the spectrometer's movable mirror. At the beamsplitter the two

12

ls-2p(m=-1) Peak Positions at 50 kilogauss

Figure 5a. 1s-2p (m= -1) peak positions at 50 kilogauss.
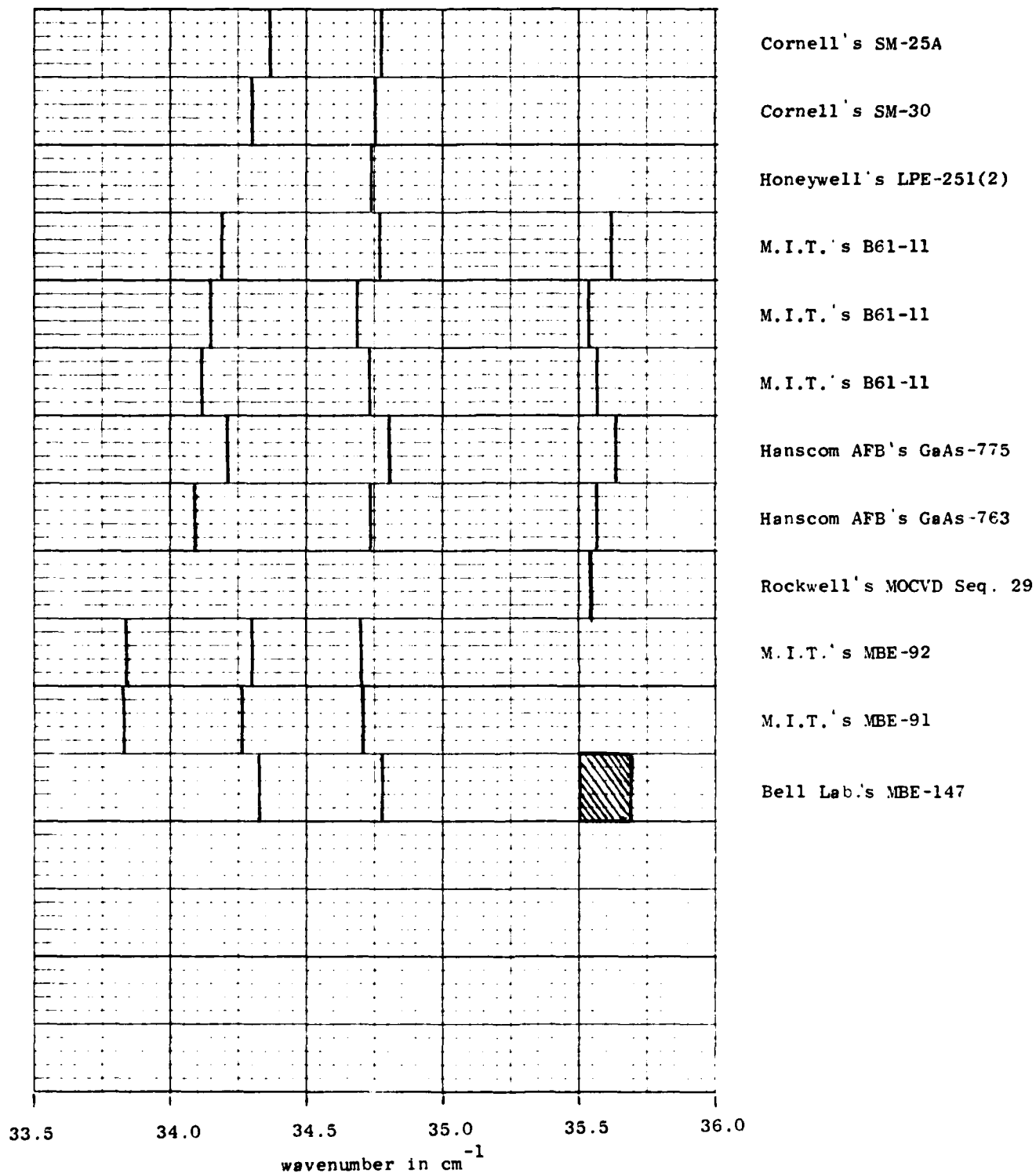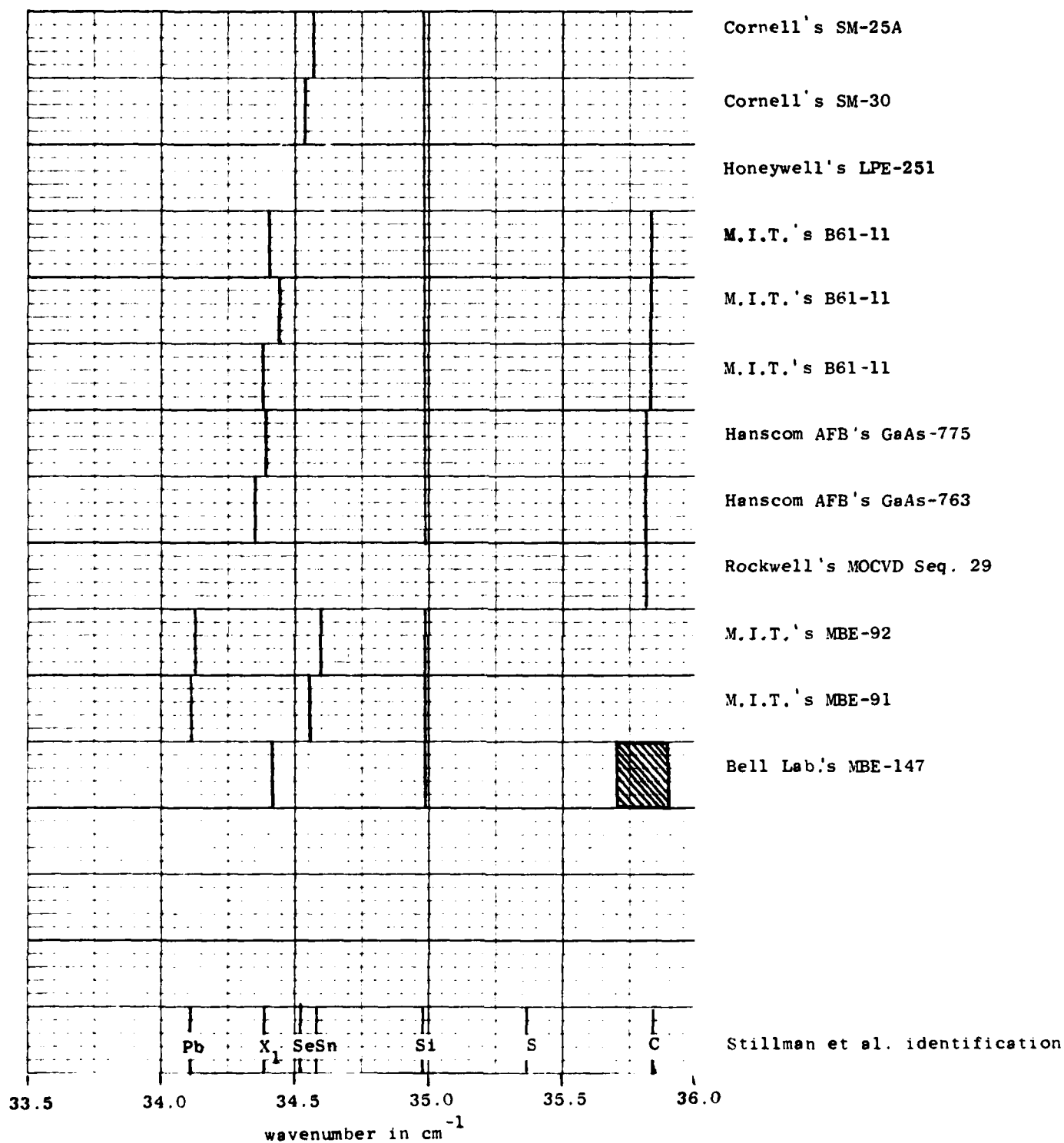
1s-2p(m=-1) Peak Positions at 50 kilogauss*

* For each run the peaks have been shifted so that the Si peak agrees with Stillman's
identification to account for slight variations in magnetic field from run to run.

Figure 5b.   1s-2p (m= -1) peak positions at 50 kilogauss*
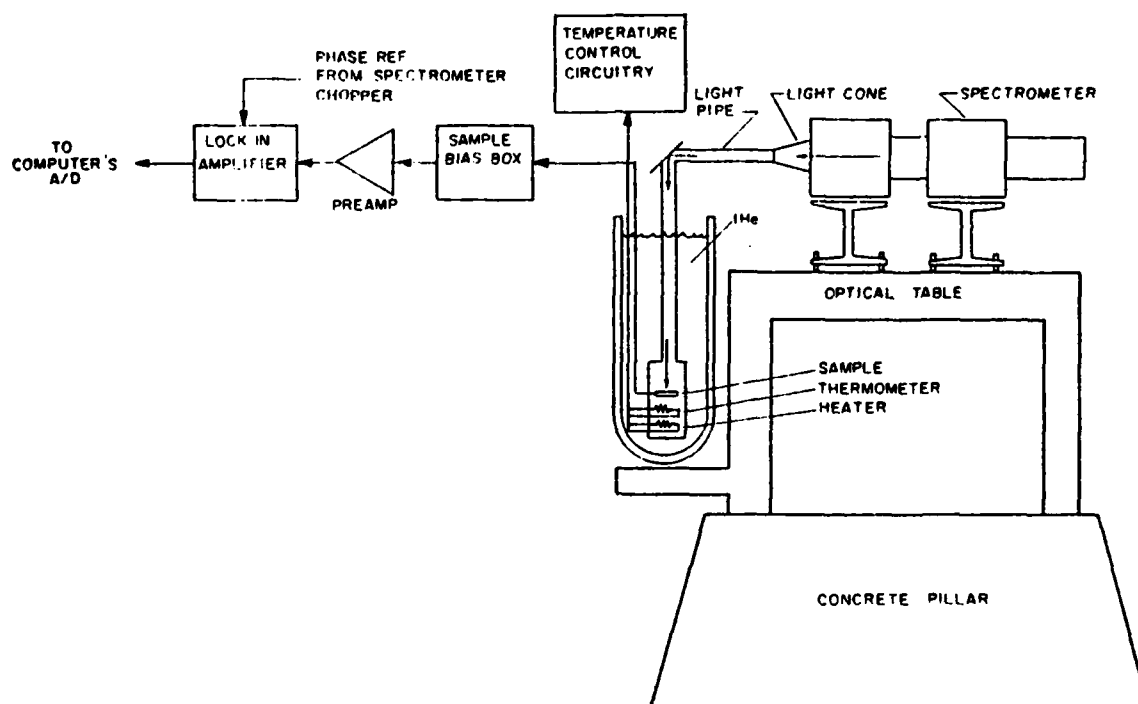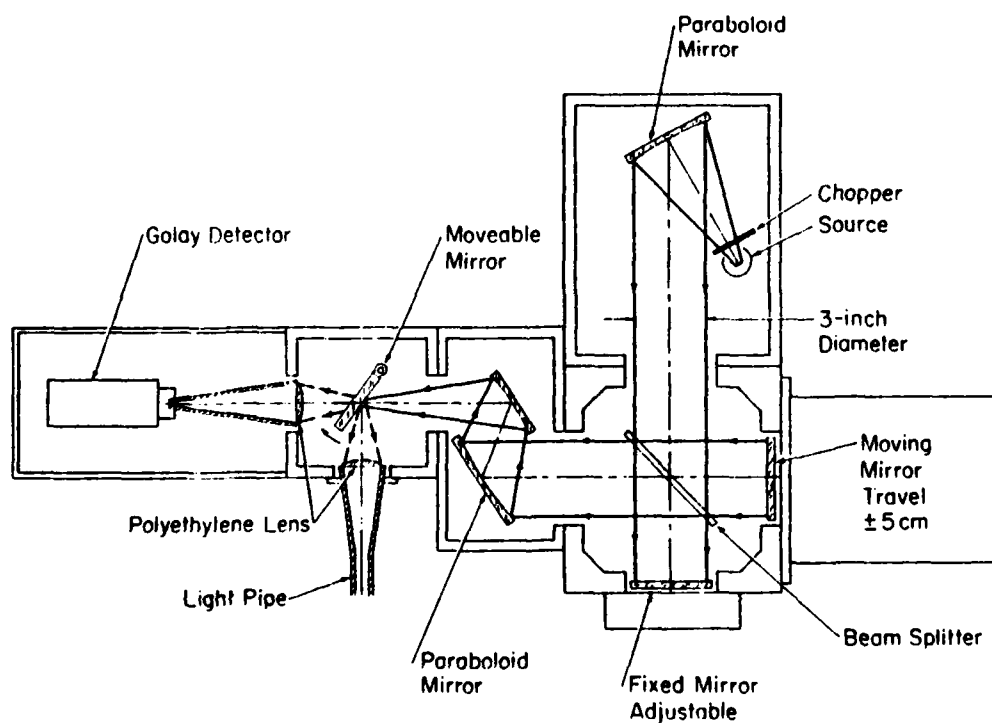
14

APPARATUS BLOCK DIAGRAM

Figure 6 (a)

Figure 6 (b)

Figure 6. Apparatus block diagram.

beams recombine and are directed to the sample by means of light pipes.
When the path difference is zero, the two beams have the same phase for all
wavelengths and the recombined beam's intensity is a maximum. For a mono-
chromatic source at wave number $\bar{\nu}$ and beams of equal intensity $S_{\bar{\nu}}$, the combined
beam intensity as a function of path difference x is given by

(4) $\qquad S(x) = S_{\bar{\nu}} (1+\cos(2\pi\bar{\nu}x))$

The photoconductivity signal at the sample is then given by

(5) $\qquad I_{\nu}(x) = R(\bar{\nu}) [T_{\bar{\nu}}S_{\bar{\nu}}(1+\cos(2\pi\bar{\nu}x))]$

where $T_{\bar{\nu}}$ is the total transmission of the spectrometer optics (filters, beam-
splitter efficiency, etc.) and $R(\bar{\nu})$ is the object of interest, the responsivity
of the sample at wavenumber $\bar{\nu}$. Since the source emits a continuous spectral
distribution $S(\bar{\nu})$ the total photoconductivity signal is given by an integral
over all wavenumbers.

$$I(x) = \int_{0}^{\infty} R(\bar{\nu})S(\bar{\nu})T(\bar{\nu})[1+\cos(2\pi\bar{\nu}x)]d\bar{\nu}$$

The Fourier cosine transform of this expression gives:

(6) $\qquad R(\bar{\nu})S(\bar{\nu})T(\bar{\nu}) = 2 \int_{-\infty}^{\infty} [I(x)-I(0)/2]e^{-i2\pi\bar{\nu}x}dx$

$$= 4 \int_{0}^{\infty} [I(x)-I(0)/2]\cos(2\pi\bar{\nu}x)dx$$

The interferogram I(x) is the quantity measured experimentally by recording
photoconductivity signal as a function of mirror position. The product
$S(\bar{\nu})T(\bar{\nu})$ can be established using (6) by a measurement taken with a detector
of known or flat responsivity. The responsivity of the semiconductor sample
$R(\bar{\nu})$ then is essentially the Fourier transform of the recorded interferogram
$I(x)$.

16

To record the interferogram, the biased sample is illuminated with
light from the spectrometer which is chopped at 150 Hz. The ac component
of the voltage across the sample is proportional to the difference in
sample conductivity with the light on from that with the light off.
This signal is amplified and fed to a lock-in amplifier referenced with a
signal from the spectrometer's chopper. Each time the LSI-11 interface
receives a pulse from the Moiré grating electronics in the spectrometer
(indicating that a specified Δx in mirror position has been traversed)
the LSI-11 records the lock-in output through an A/D converter as one data
point in the interferogram. The spectrometer mirror is in continuous motion
at speed v and the lock-in amplifier's time constant is chosen to be comparable
to the time between digitize pulses $\Delta x/v$. The recorded lock-in output then
is an average of the photoconductivity amplitude over the last Δx of mirror
travel. Evidently from equation (4), Δx is to be chosen to be at least
as small as $1/(2 \bar{\nu}_{max})$ where $\bar{\nu}_{max}$ is the largest wavenumber of interest. When
a certain predetermined number of data points have been recorded (typically
4096), the completed interferogram is stored on the LSI-11's floppy disc.
The interferogram can be quickly displayed on a graphics terminal, or, if
hard copy is desired, it can be permanently recorded on an x-y plotter.
An example of such an interferogram plot is shown in Fig.7.

After it is recorded, mathematical operations on the interferogram data
can be performed by the LSI-11 leading to a spectrum of photoconductive
response versus wavenumber. These operations may include removal of noise
spikes, slope or D.C. shift in the interferogram, apodization, zero filling,
etc., but the essential operation is a discrete Fourier transform (DFT)
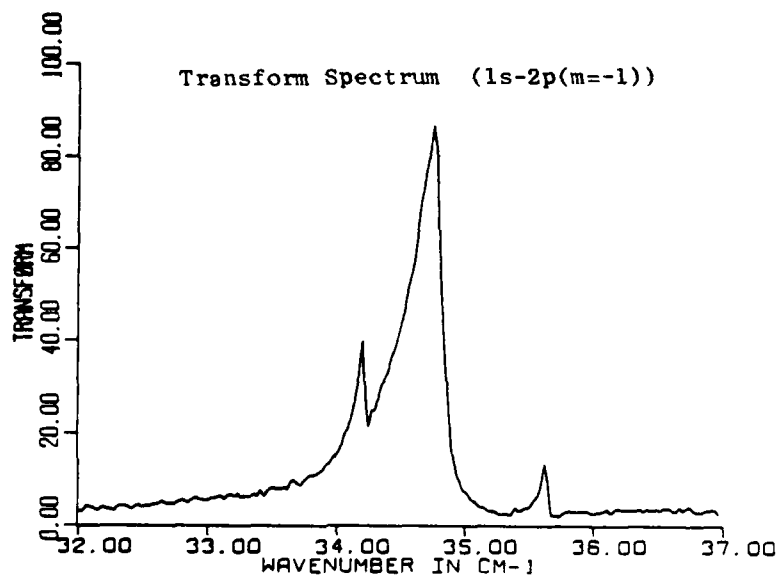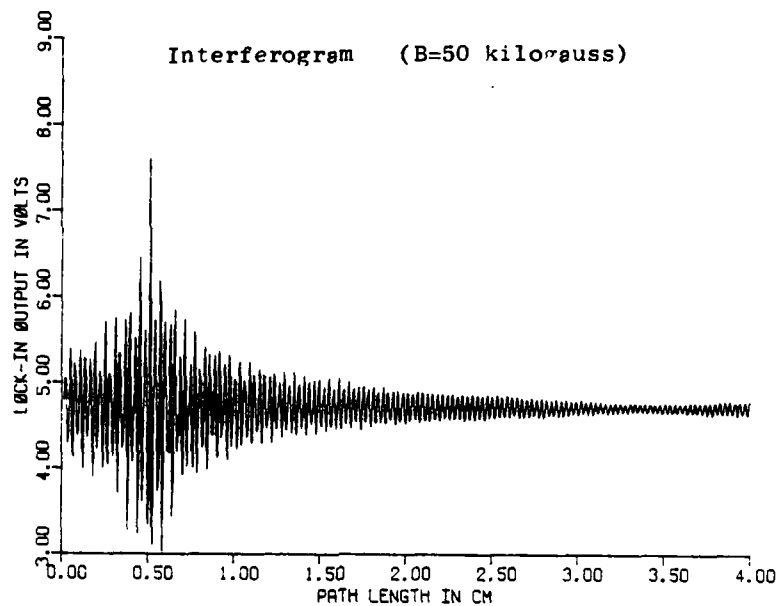of the interferogram.

17

Figure 7.   Typical interferogram and transform spectrum from the apparatus.

18

The photoresponse of the sample $R(\bar{\nu})$ is related to the interferogram $I(x)$ through equation (6).

$$(7) \qquad R(\bar{\nu})S(\bar{\nu})T(\bar{\nu}) = 4 \int_{0}^{\infty} [I(x)-I(0)/2]\cos(2\pi\bar{\nu}x)dx$$

$$= 4 \ \mathrm{Re}\{\int_{0}^{\infty} [I(x)-I(0)/2]e^{-i2\pi\bar{\nu}x}dx\}$$

Since all calculations are to be performed by a digital computer (the LSI-11 in our case), $I(x)$ is sampled at discrete values x_n over a finite interval ($x_n = nD/(N-1)$ $n = 0, 1, \ldots N-1$) and a discrete approximation to the above integral,

$$(8) \qquad R(\bar{\nu})S(\bar{\nu})T(\bar{\nu}) \rightarrow 4 \ \mathrm{Re}\{\sum_{n=o}^{N-1} [I(x_n)-I(0)/2]e^{-i2\pi\bar{\nu}x_n} \Delta x_n\}$$

$$= 4(D/(N-1))\mathrm{Re}\{\sum_{n=o}^{N-1} [I(x_n)-I(0)/2]e^{-i2\pi\bar{\nu}x_n}\}$$

must be used.

The quantity $R(\bar{\nu})S(\bar{\nu})T(\bar{\nu})$ is calculated only at N discrete values $\bar{\nu}_k$ ($\bar{\nu}_k = k/D$ $k=0, 1, \ldots, N-1$). With the definition $e^{-i2\pi/N} \equiv W_n$, equation (8) can be written as

$$(9) \qquad R(\bar{\nu}_k)S(\bar{\nu}_k)T(\bar{\nu}_k) = 4 \ (D/(N-1)\mathrm{Re}\{\sum_{n=o}^{N-1} [I(x_n)-I(0)/2]W_N^{nk}\} \ .$$

If we define $[I(x_n)-I(0)/2] \equiv a(n)$ and

$$R(\bar{\nu}_k)S(\bar{\nu}_k)T(\bar{\nu}_k)/(4D/(N-1)) \equiv \mathrm{Re}[A(k)]$$

then (9) can be written

$$(10) \qquad A(k) = \sum_{n=o}^{N-1} a(n) \ W_N^{+nk} \ .$$

19

Thus A(k), which is proportional to the photoresponse of the sample, is the DFT of the interferogram a(n). The inverse transform is just

(11) $\qquad a(n) = \frac{1}{N} \sum_{k=0}^{N-1} A(k) W_N^{-nk}$.

It has been tacitly assumed in all of the above discussion that the point where the path difference in the spectrometer is zero is $x_n = 0$ which corresponds to the zeroth sampled point in the interferogram. This is not the case experimentally. The mirror position of zero path difference (ZPD) will lie at some $x_{ZPD} : 0 \leq x_{ZPD} \leq D$ and in general will lie between sampled interferogram points (See Fig.8). Thus the analysis should proceed from equation (4) being changed to read:

$$S(x) = S_{\bar{\nu}} (1 + \cos 2\pi \bar{\nu}(x - x_{ZPD})).$$

For a continuous Fourier transform the fact that $x_{ZPD} \neq 0$ presents no problem since by a change of variables

(12) $\qquad \int_{-\infty}^{\infty} I(x - x_{ZPD}) e^{-i2\pi\bar{\nu}x} dx = e^{-i2\pi\bar{\nu}x_{ZPD}} \int_{-\infty}^{\infty} I(x) e^{-i2\pi\bar{\nu}x} dx$.

We can then correct for the fact that zero path difference was not at x=0 simply by knowing x_{ZPD} and multiplying by an exponential factor. However, in sampling the interferogram discretely, if a measurement is not taken at x_{ZPD} (as is generally the case), serious distortions can appear in the computed DFT spectrum. Such distortion is representative of one class of phase error, and there are a number of phase correction schemes designed to eliminate this problem.

phase error $I(x_n)-I(0)/2$
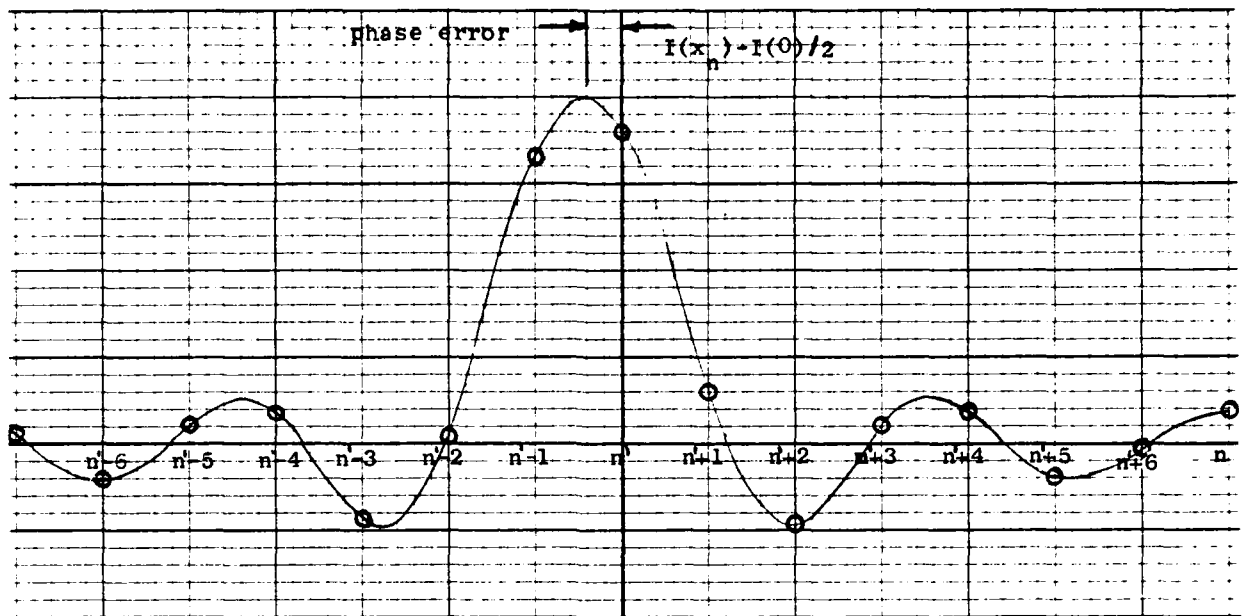
Shown is an example of a hypothetical interferogram in which no sample
point occurs at zero path difference. Note the resulting asymmetry in
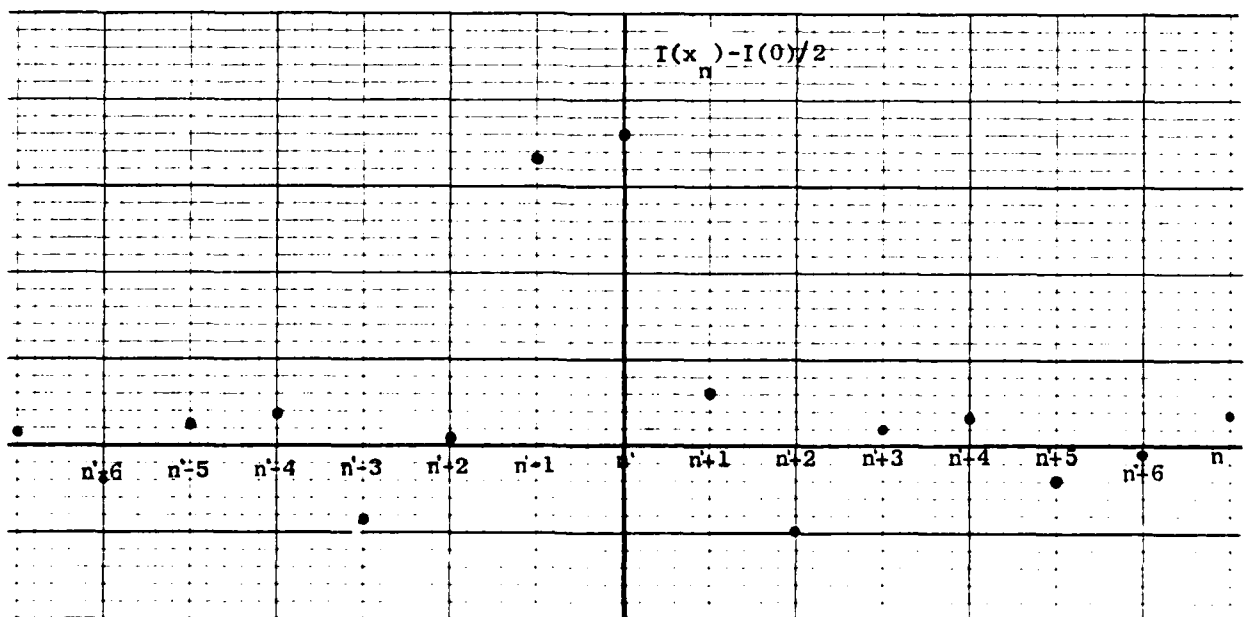the digitized interferogram below.

$I(x_n)-I(0)/2$

Figure 8. Graphic representation of a course of error.

21

Two such phase correction schemes have been applied by us to both experimentally obtained and synthetic interferograms. Their effects on spectral line widths and line shapes have been compared for a variety of different synthetic interferograms.

The first phase correction method is extremely simple and can be understood by examining equation (12). Since the interferogram is symmetric about x_{ZPD} the Fourier transform with respect to an origin at x_{ZPD} is real and equal to the modulus of either side of equation (12). Thus the first means of phase correction consists of taking the full complex DFT of $[I(x_n)-I(0)/2]]$ and then taking the modulus of the result.

Another method of phase correction we have studied is similar to that described by Mertz.[8] In this scheme the full complex DFT of the severely apodized interferogram is computed and the phase of this specturm ϕ_s is recorded. Severe apodization is accomplished by multiplying the interferogram $[(I(x_n)-I(0)/2]$ by a function $a_s(x)$ of the form (See Fig.9(a).)

$$(13) \qquad a_s(x) = 1 - \frac{|x-x_{max}|}{x_A} \text{ for } |x| \leq x_A$$

$$= 0 \text{ for } |x| > x_A$$

where $x_a << D$ and x_{max} is the position of the interferogram maximum (which is presumably within $D/(N-1)$ of x_{ZPD}). The phase ϕ_s constitutes an average or reference phase indicative of the position of the true zero path difference x_{ZPD}. Then the full complex DFT of the normally apodized interferogram is computed. Normal apodization is accomplished by multiplying the interferogram by $a_n(x)$. (See Fig. 9(b).) This functional form of $a_n(x)$ is chosen so that the redundant information on either side of $x_{max} \doteq x_{ZPD}$ is not double counted. Finally, the phase corrected spectrum $A_{corrected}(k)$ is computed by

22
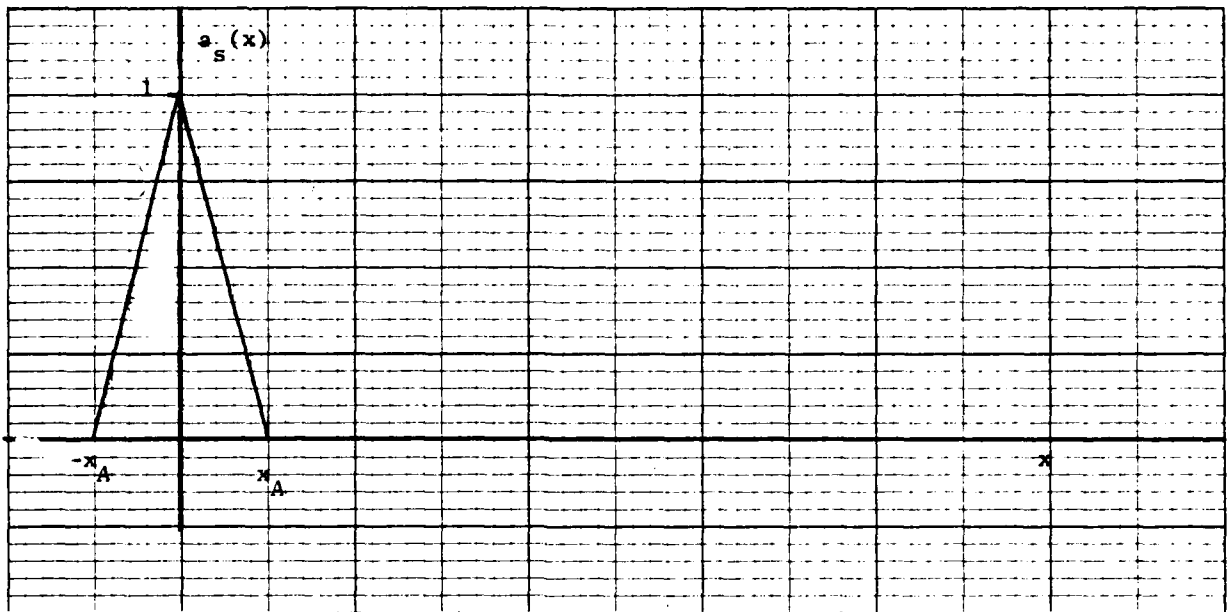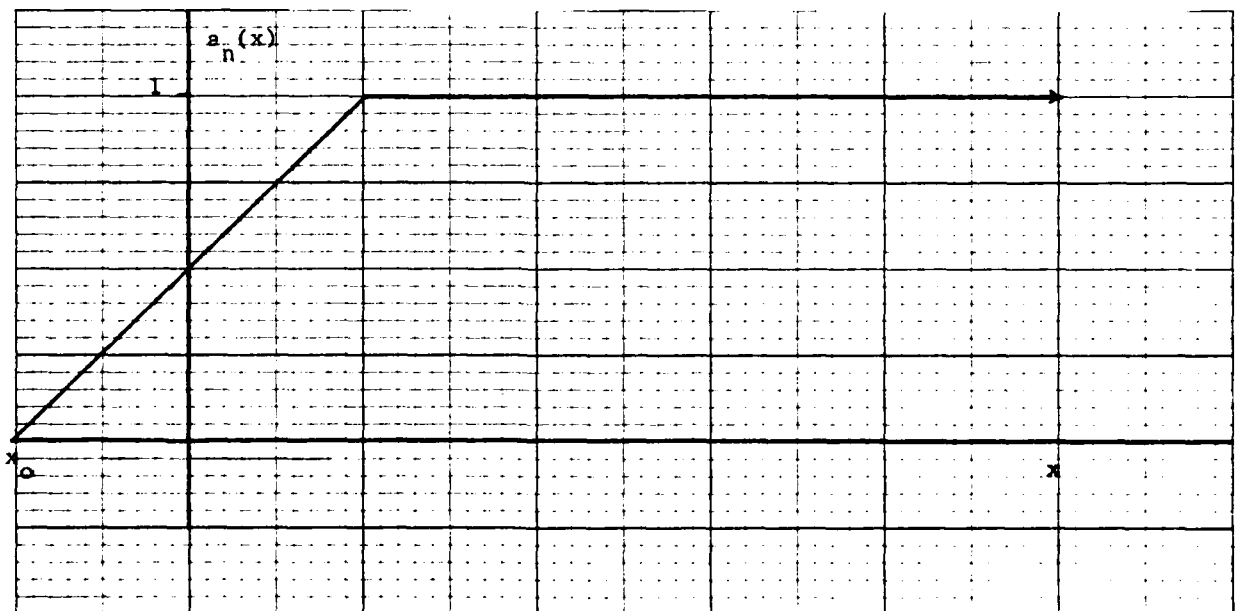
Figure 9 (a)

Figure 9 (b)

Figure 9. Apodization functions.

(14) $$A_{corrected}(k) = Re\{A(k)e^{-i\phi}s\} \quad .$$

It can be shown that if $a_s(x)$ were chosen to be a symmetric box about x_{max} then the method described above is exactly equivalent to the method described by Mertz.

For the study of impurity-impurity interactions through line shapes in the photothermal ionization spectra, it is essential to ascertain and minimize any effect of the digital Fourier transformation technique on those line shapes. In order to compare the two phase correction schemes described above, and in particular their effect on spectral line shape, a program was written to generate synthetic interferograms. These are digitally sampled finite path difference subsets of a continuous function whose Fourier integral transform is a wedge of the form

(15)
$$f(\bar{\nu}) = 0 \qquad \qquad \bar{\nu} < \bar{\nu}_1$$

$$f(\bar{\nu}) = +A(\bar{\nu}-\nu_1)/(\bar{\nu}_2-\bar{\nu}_1) \qquad \bar{\nu}_1 \leq \bar{\nu} \leq \bar{\nu}_2$$

$$f(\bar{\nu}) = -A(\bar{\nu}-\bar{\nu}_3)/(\bar{\nu}_3-\bar{\nu}_2) \qquad \bar{\nu}_2 \leq \bar{\nu} \leq \bar{\nu}_3$$

$$f(\bar{\nu}) = 0 \qquad \qquad \bar{\nu}_3 < \bar{\nu} \quad .$$

The form of this function was chosen to simulate the characteristic line shape observed in the 1s-2p (m=-1) transitions in GaAs. The synthetic interferograms were generated using various sampling parameters typical of those used experimentally. Also, and most important from the standpoint of comparing phase correction methods, interferograms were generated with various amounts of phase error. That is, the distance from the continuous interferogram's maximum to the nearest sampled point was varied. (See Fig. 8.) The discrete

Fourier transforms of these synthetic interferograms were then computed and the resulting spectra compared.

In an interferogram from a well aligned spectrometer, the data are symmetric about x_{ZPD}. All the information is contained in one or the other halves of the interferogram and so recording both halves is a waste of time and computer memory. Also, the resolution $\Delta\bar{\nu}$ (cm^{-1}) of the computed spectrum is given by

$$(16) \qquad \Delta\bar{\nu} = \frac{1}{D}.$$

where D (cm) is the maximum optical path difference achieved by the spectrometer's movable mirror during the recording of the interferogram. In high resolution spectra, to minimize $\Delta\bar{\nu}$, D is chosen as large as possible. The mirror drive in the spectrometer can move the mirror a maximum of 10 cm which corresponds to an optical path difference change of 20 cm. To improve resolution, the spectrometer has been modified in such a way as to move x_{ZPD} from a mirror position near the middle of the mirror drive travel to a position near one end. This allows the recording of one-sided interferograms with a D of nearly 20 cm and with a corresponding resolution of about 0.05 cm^{-1}. With these one-sided interferograms, proper phase correction is a necessity. Our synthetic interferograms have been constructed to simulate the experimentally recorded interferograms, having $x_{ZPD}=0.48$ cm and D=18.0 cm. The number of sample points N and sample interval Δx were N=3850 and $\Delta x=48$ microns.

Table III summarizes the sampling parameters and phase error information and figures 10 through 15 show some of the resulting spectra. The labels "modulus spectrum" and "phase referenced spectrum" indicate that, respectively, the first and second of the above described phase correction methods were

25

TABLE III. SYNTHETIC INTERFEROGRAM PARAMETERS.

Interferogram	NPTS	$\Delta x(\mu m)$	$x_{ZPD}/\Delta x$	Phase Error/Δx	$\bar{\nu}_1(cm^{-1})$	$\bar{\nu}_2(cm^{-1})$	$\bar{\nu}_3(cm^{-1})$
0	3850	48	100	0.5	35.0	36.0	36.5
6	3850	48	100	0.5	35.75	36.00	36.00
7	3850	48	19.26	0.5	35.75	36.00	36.00
10	3850	48	100	0.05	35.0	36.0	36.0
11	3850	48	100	0.1	35.0	36.0	36.0
12	3850	48	100	0.3	35.0	36.0	36.0
13	3850	48	100	0.5	35.0	36.0	36.0

NPTS = no. of interferogram sample points

Δx = sample interval

x_{ZPD} = position of zero path difference

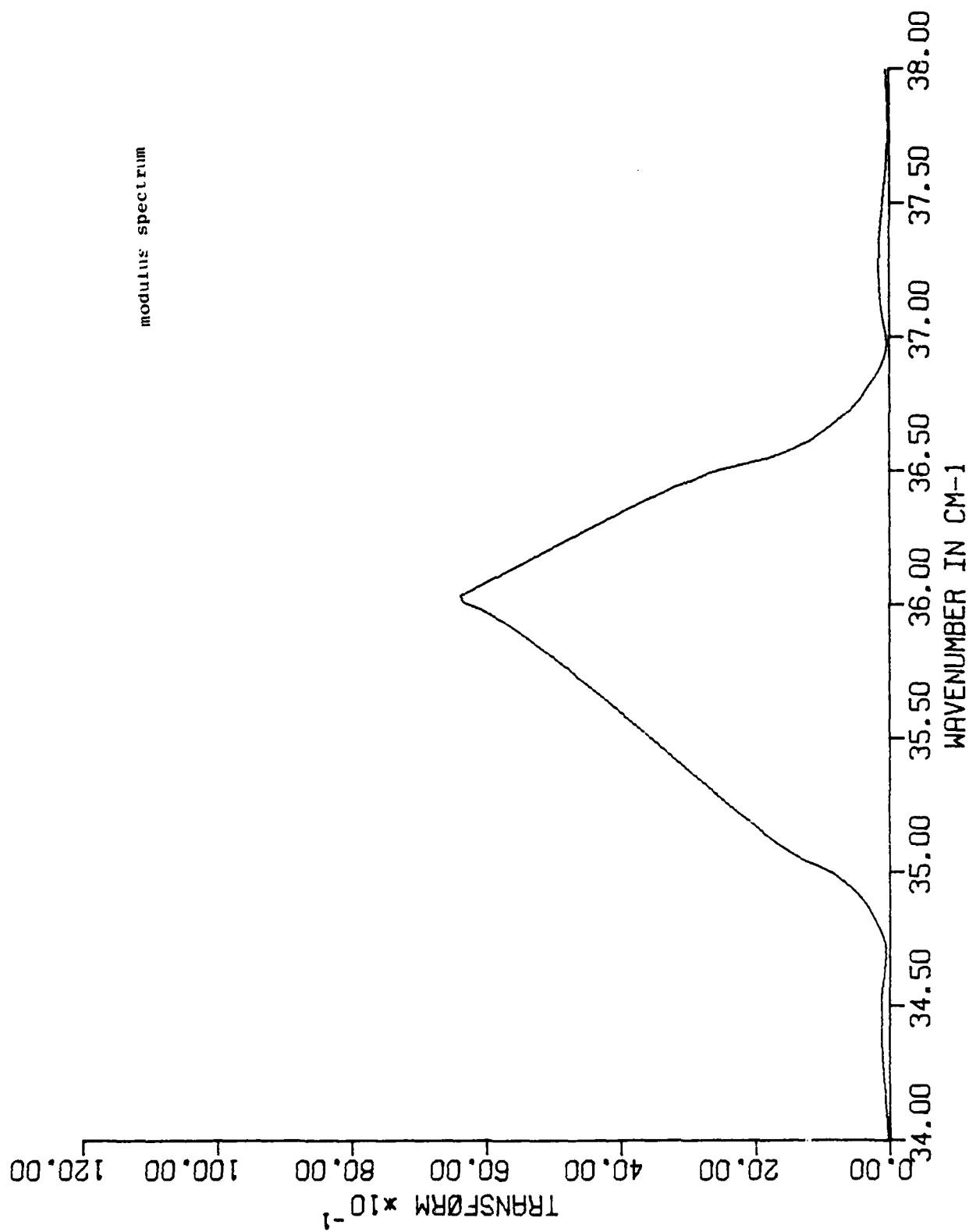Phase error = distance from x_{ZPD} to nearest sample point

modulus spectrum

Figure 10. Modulus spectrum of synthetic interferogram.

27

phase referenced spectrum

WAVENUMBER IN CM-1

TRANSFORM ×10⁻¹
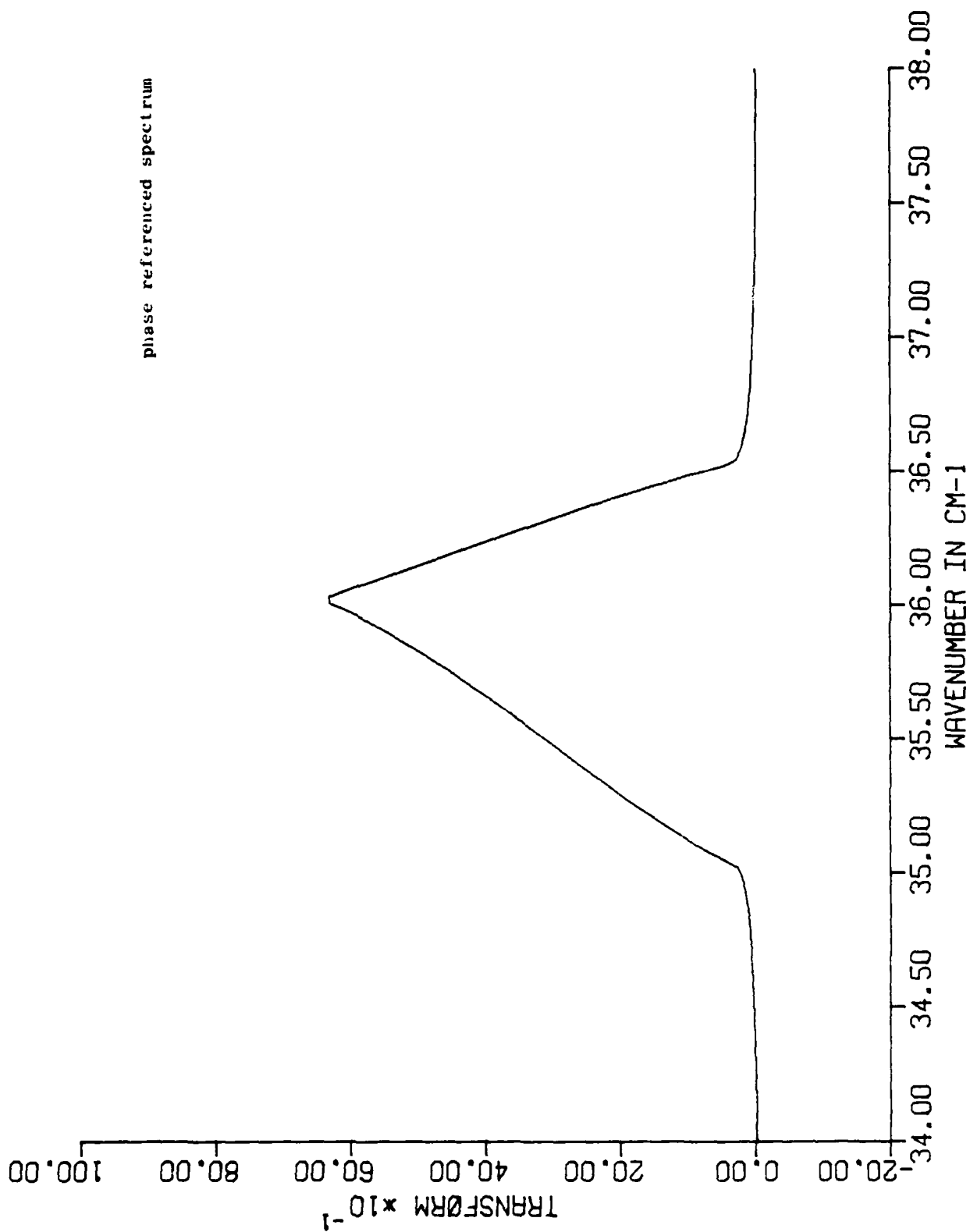
Figure 11. Phase referenced spectrum of synthetic interferogram 0.

28
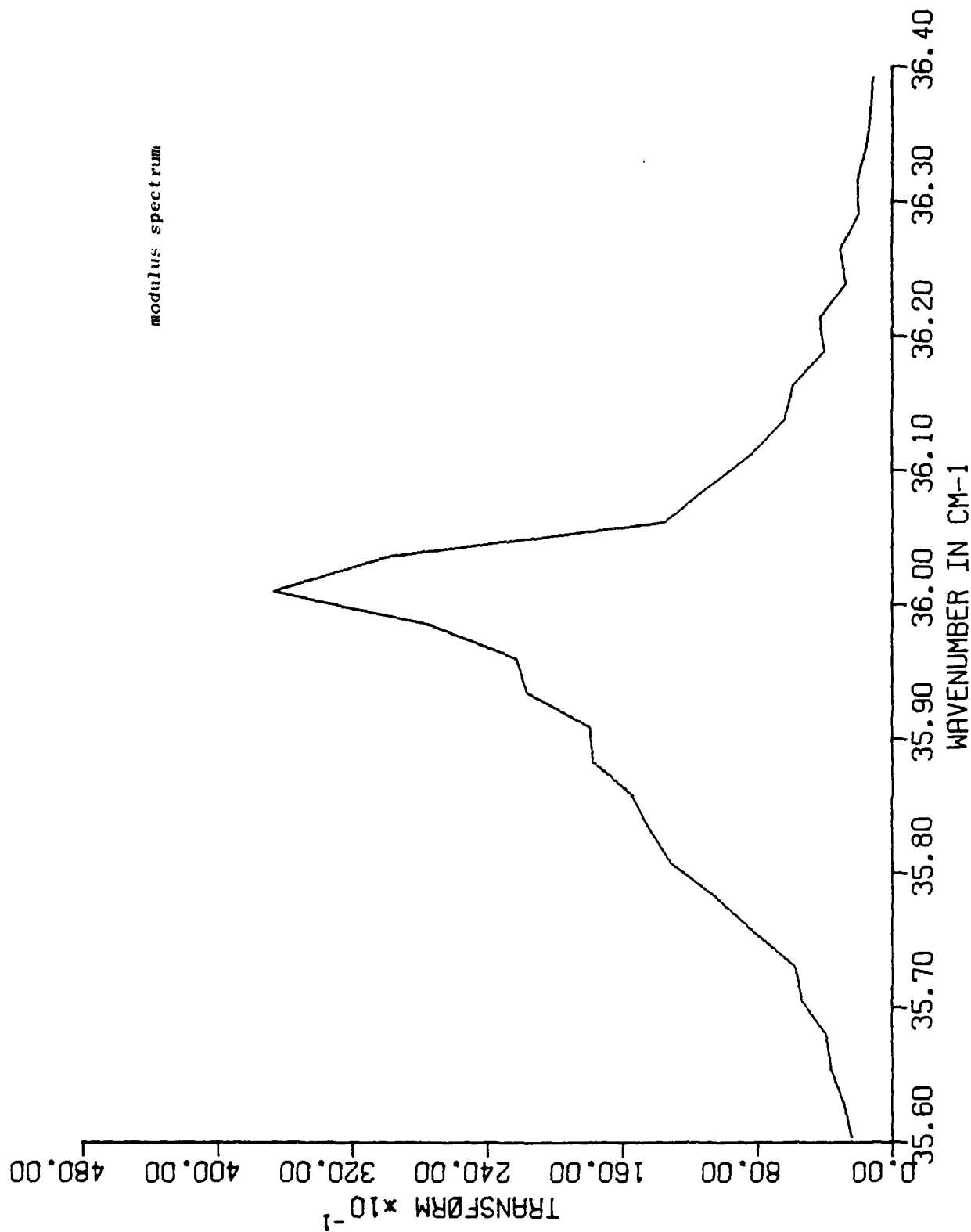
Figure 12. Modulus spectrum of synthetic interferogram 7.

phase referenced spectrum

TRANSFORM ×10^{-1}

WAVENUMBER IN CM-1

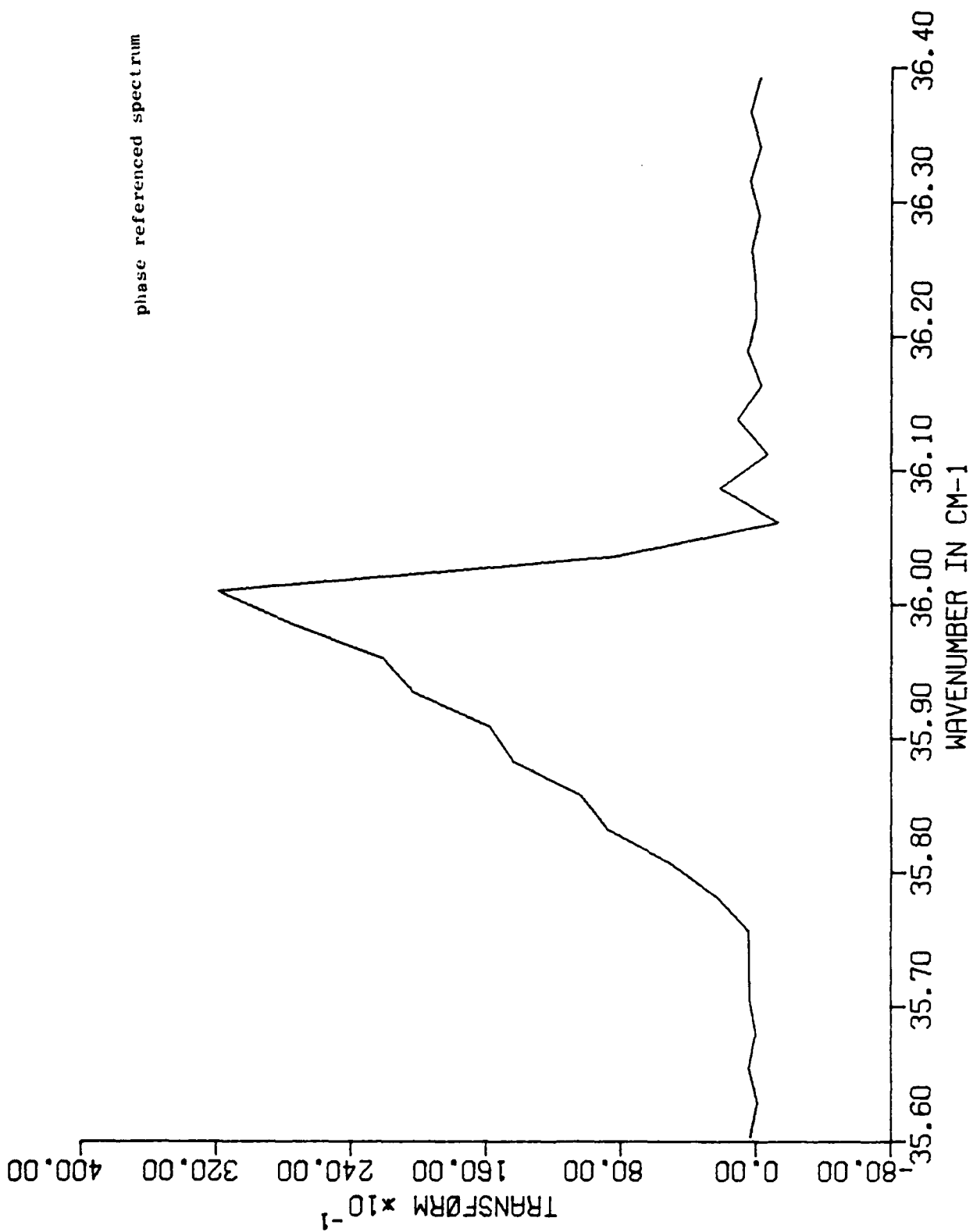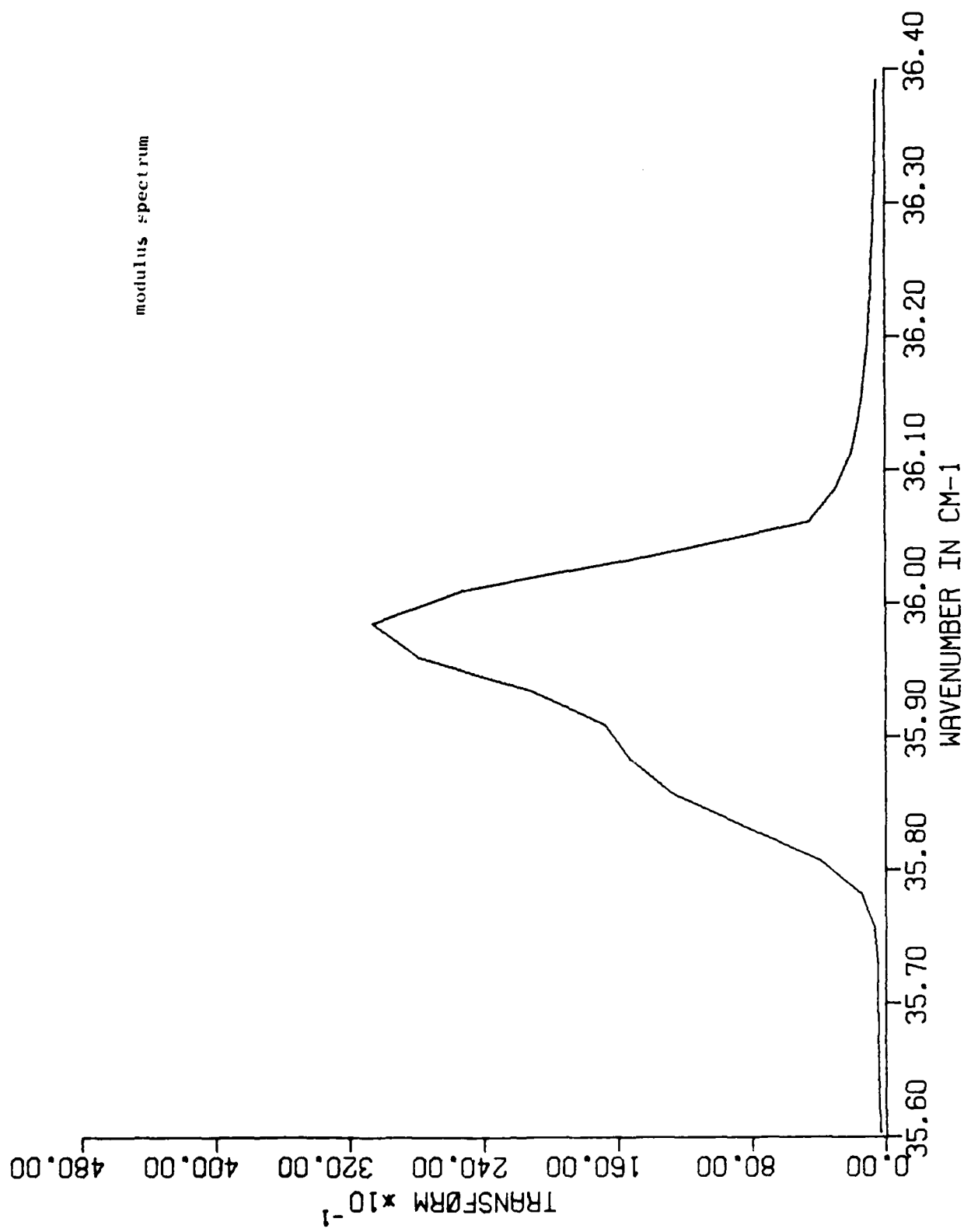Figure 13. Phase referenced spectrum of synthetic interferogram 7.

30

Figure 14. Modulus spectrum of synthetic interferogram 6.
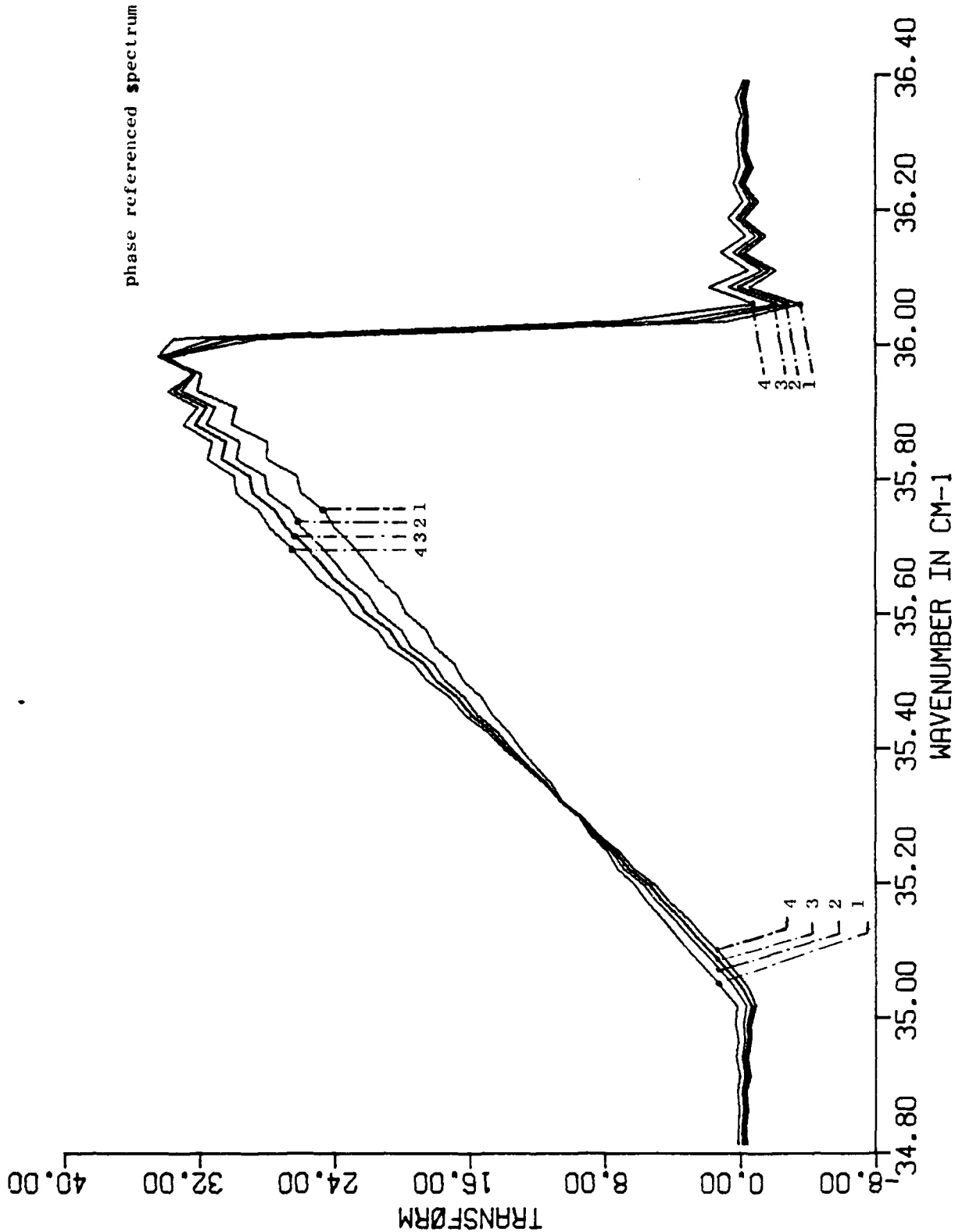
modulus spectrum

31

Figure 15. Phase referenced spectra of synthetic interferograms 10, 11, 12, and 13 (marked 1, 2, 3, and 4, respectively.)

employed in computing that spectrum. Notice that in all these spectra, as in the experimental spectra, the line widths are extremely narrow, being from .014 to .007 of the wavenumber at which they occur.

Figures 10 and 11 are respectively the modulus and phase referenced transforms of interferogram 0 which has $\bar{v}_1 = 35.0$ cm^{-1}, $\bar{v}_2 = 36.0$ cm^{-1}, and $\bar{v}_3 = 36.5$ cm^{-1}. A perfect undistorted transform of this interferogram would be a triangular wedge with vertices at these wavenumbers, and both spectra approximate this. The phase error for this interferogram was 0.5 Δx which is considered a worst case.

Notice that the modulus spectrum is the poorer of the two approximations to the true line shape, having too large a line width, distortion of the ideally straight sides of the triangular wedge, and broad side lobes which extend out several wavenumbers from the main peak. These side lobes are not the ones usually associated with unapodized spectra, having a period which is far too large to be accounted for in this way.

The phase referenced spectrum is a considerably closer approximation to the ideal line shape but it too is slightly distorted. The side lobes apparent in the modulus spectrum are absent here, but the distortion in the main body of the peak is similar in character though much reduced. The line width in the phase referenced spectrum is correct and the only distortion away from the main peak is a slight upward curvature of the baseline as the peak is approached from either side.

The line width of interferogram 0 is considerably larger than one encounters in the purest GaAs available. In Fig. 22 for example, the spectrum of B61-11 has line widths of order 0.1 cm^{-1}. With this in mind, interferogram 7

33

was prepared with $\bar{\nu}_1 = 35.75$, $\bar{\nu}_2 = 36.00$, $\bar{\nu}_3 = 36.00$, and a phase error of 0.5 Δx.
The modulus and phase referenced spectrum of this interferogram are shown
respectively in figures 12 and 13.

Again the modulus spectrum represents the poorer approximation to the
true line shape. Its line width is too large and the ideal precipitous drop
in amplitude at high wavenumber is smeared into a gradual decline. The
sidelobes, although not apparent in the figure, were present with amplitude
of about 0.02 that of the main peak. There is a pronounced peaking at the
apex of the line and a gross distortion of the ideal right triangular
peak shape.

The phase referenced spectrum is a much closer approximation to the
true line shape. The most obvious deviations are the Gibbs oscillations
around the high wavenumber edge of the peak which were mentioned above.
The ideal precipitous drop in amplitude at $\bar{\nu}_2$ is again smeared, but this time
only over a wavenumber range equal to the resolution $\Delta\bar{\nu} = .05$ cm^{-1}. The low
energy side of the peak is slightly concave from above and contains the Gibbs
oscillations, but it is a fairly good approximation to the true line shape.
Interferogram 7 was prepared identically to interferogram 6 except that x_{ZPD}
was placed in the middle of interferogram 7. The modulus spectrum of 7 is
shown in Fig. 14. Because the distance from x_{ZPD} to the extremes of the inter-
ferogram has been halved, the resolution of the spectrum is likewise halved,
but it is interesting to note that the line shape and line width are nearly as
good as those of the phase referenced spectrum of interferogram 6.

Finally, interferograms 10, 11, 12 and 13 were prepared to investigate
the size and nature of the effect of phase error on lineshape. All four
interferograms are identical having $\bar{\nu}_1 = 35.0$, $\bar{\nu}_2 - 36.0$, and $\bar{\nu}_3 = 36.0$ except for
their phase errors which in units of the sampling interval Δx are 0.05, 0.1,

34

0.3 and 0.5 respectively. Figure 15 is a plot of the phase referenced spectra of these interferograms which are labeled respectively, 1, 2, 3 and 4. As the phase error is increased, that is, as the closest sample point to x_{ZPD} is moved progressively further away from x_{ZPD}, the distortion of the true line shape becomes worse until at a phase error of 0.5 it is at a maximum. The maximum deviation from the ideal line shape is about 10% of the peak amplitude and this might well be significant if one were examining line shapes to study impurity interactions. We are currently investigating possible means for reducing this distortion further.

EXPERIMENTAL WORK

Several samples of high purity GaAs grown by various industrial and government laboratories have been measured using the photothermal ionization technique. These samples are representative of the best quality material which can presently be grown by various growth techniques. Hall effect measurements at 77 K in a field of 6 kilogauss have determined the mobility μ_{77} and donor and acceptor impurity concentrations (N_D and N_A, respectively) in all of these samples. (See Table IV.) By examining the 1s-2p(m=-1) peak positions in the 50 kilogauss spectra of these samples and comparing with the identifications of Wolfe, Stillman, and Korn[3], we have established the residual donor species present in these samples. The correlation between residual donors present and growth technique for samples grown in different laboratories suggests that the residual donors we have identified may be characteristic of the associated growth technique.

MBE SAMPLES

Three samples grown by molecular beam epitaxy (MBE) were measured. The first of these, MBE A-147, was grown by A.Y. Cho and H. Morkoç at Bell Labs.

TABLE IV. HALL DATA AND PEAK IDENTIFICATIONS FOR PHOTOTHERMAL IONIZATION SAMPLES.

Sample #	$\mu_{77}(cm^2/Vsec)$	$N_D(cm^{-3})$	$N_A(cm^{-3})$	Peak ID's and linewidths (cm^{-1}) at 50 kilogauss			
MBE A-147	81,246	$6.65x10^{14}$	$2.65x10^{14}$		(SeSn).48	Si.13	C-
MBE-91	97,728	$5.08x10^{14}$	$2.96x10^{14}$	Pb.20 X_1.26	(SeSn).26	Si.18	
MBE-92	140,468	$2.15x10^{14}$	$8.73x10^{13}$	Pb.20 X_1 ?	(SeSn).18	Si.16	
Seq. 29	78,325	$6.11x10^{14}$	$5.21x10^{14}$			Si -	C.31
Seq. 129	99,066	$3.82x10^{14}$	$3.12x10^{14}$				
Seq. 132	98,118	$6.11x10^{14}$	$2.56x10^{14}$	X_1.20		Si.20	C.40
B61-11	200,993	$5.41x10^{13}$	$9.44x10^{12}$	X_1.12		Si.09	C.06
GaAs-763	157,000	$9.71x10^{13}$	$6.81x10^{13}$	X_1.14		Si.15	C.13
GaAs-775	137,000	$1.75x10^{14}$	$1.05x10^{14}$	X_1.13		Si.21	C.07
SM-25A	129,000	$2.73x10^{14}$	$1.28x10^{14}$		(SeSn).10	Si.10	
SM-30	116,700	$3.68x10^{14}$	$1.85x10^{14}$		(SeSn).23	Si.14	
LPE-251(2)	88,010	$5.42x10^{14}$	$3.96x10^{14}$	X_1 ?	(SeSn) ?	Si.20	

The remaining samples MBE-91 and MBE-92 were grown by A.R. Calawa at MIT Lincoln Labs. Photothermal ionization spectra for these samples appear in Figures 16, 17 and 18.

The spectrum of MBE A-147 shows three distinct peaks which can be associated with known simple donor species. The first and largest of these is either Se or Sn (the 1s-2p (m=-1) transition energies for these two species being very similar). A second peak of much smaller line width occurs at higher wavenumber and is almost certainly Si. Finally, at a still higher wavenumber, a small peak attributable to C can be discerned above the noise. The relative amplitudes of these peaks give a rough indication of the relative concentration of the associated donor species. (The integrated area under each peak would be a better measure.) These peak amplitudes are in a ratio of (SeSn):Si:C:: 20.0:8.5:22.0. It is interesting to note the marked difference in line width between the (SeSn) peak and the Si peak since in the usual picture of a uniform distribution of donor and acceptor impurities the 1s-2p (m=-1) Stark broadening is expected to be the same for all donor species. This suggests the possibilities of either an additional source of broadening or a donor species dependent non-uniform distribution of charged impurities about the donor site or an otherwise inhomogeneous sample 7.

The spectra of MBE-91 and MBE-92 show the same residual impurities to be present but in rather different relative concentrations. Again as in MBE A-147,the (SeSn) and Si peaks are prominent but, in addition,Pb and possibly X_1 (seen as a shoulder on the (SeSn) peak) are present. The X_1 peak is seen in VPE material as a residual donor but to our knowledge it has never been seen in LPE material. It has been suggested that X_1 may be a Ga vacancy-impurity complex[12] but this identification must be regarded
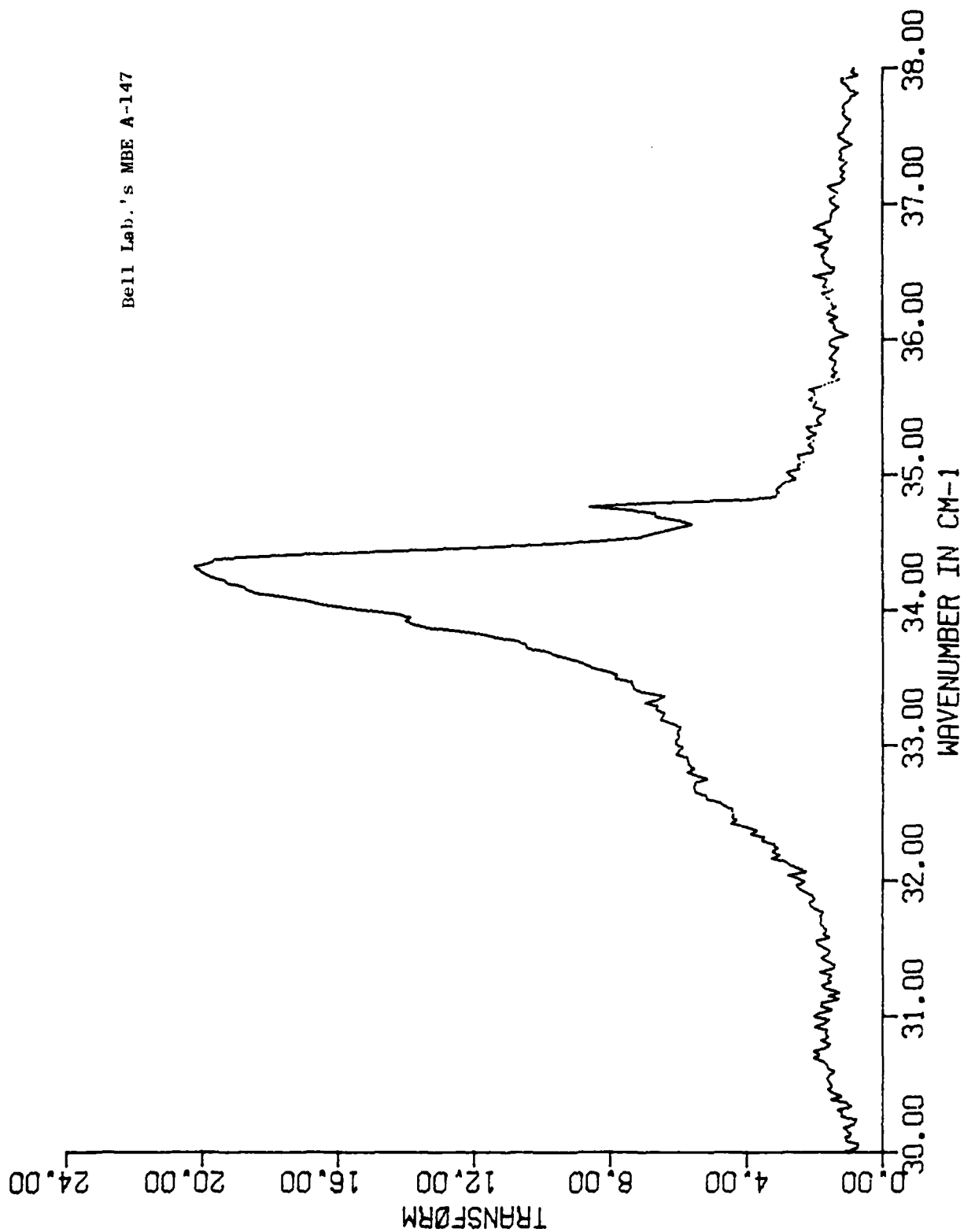
37

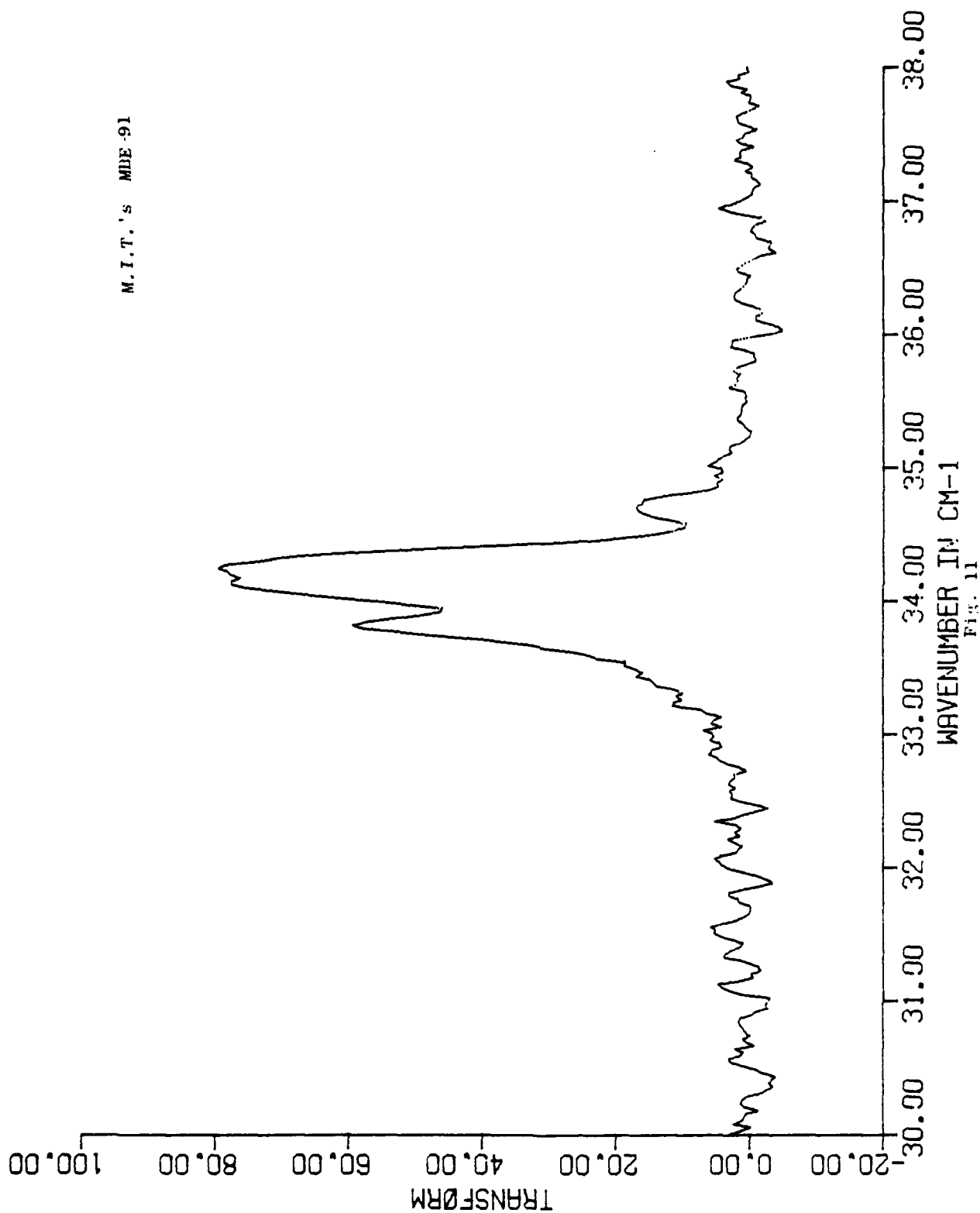Figure 16. Photothermal ionization spectrum of Bell Laboratory's MBE A-147.

Figure 17. Photothermal ionization spectrum of M.I.T.'s MBE-91.
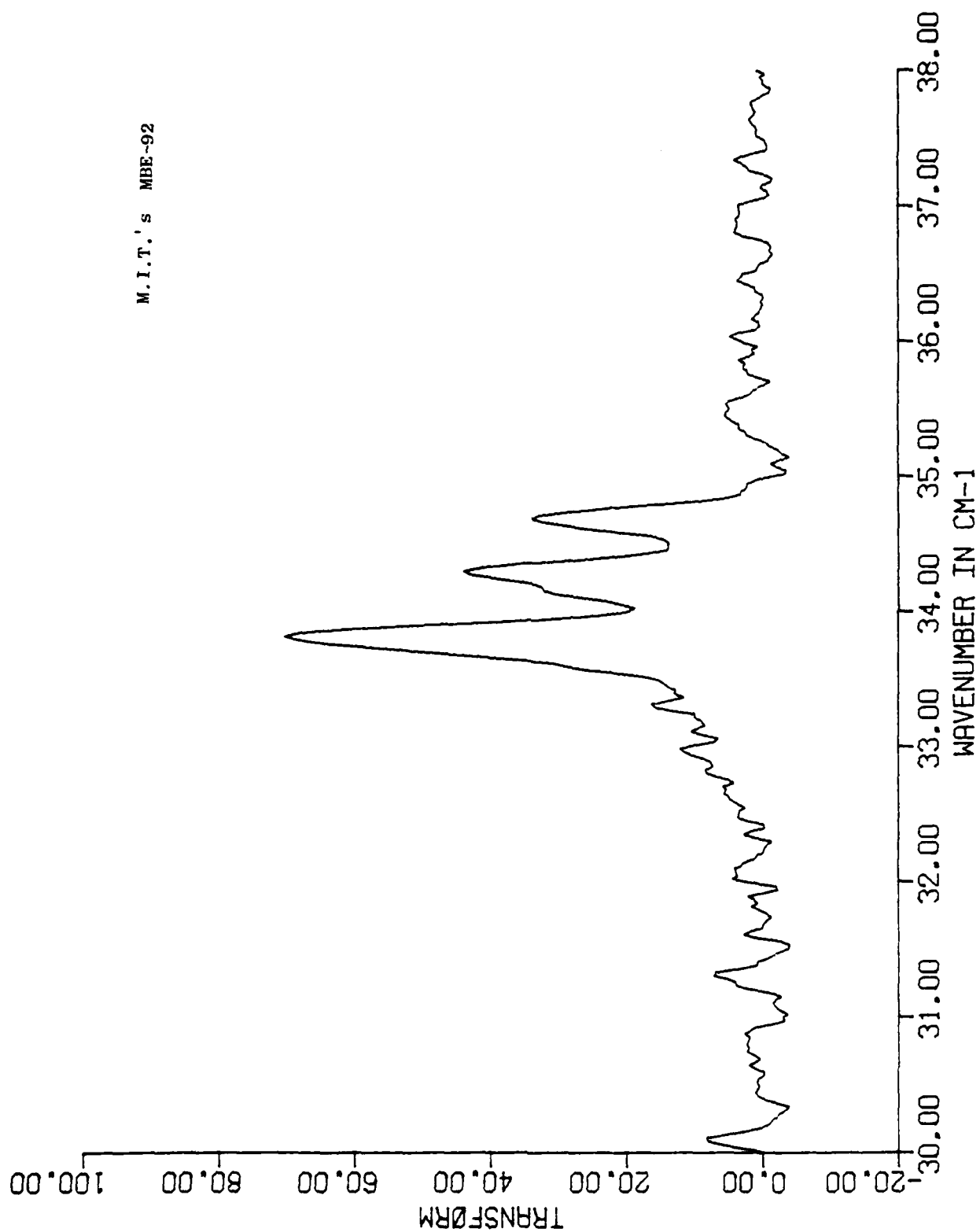
M.I.T.'s MBE-92

Figure 18.   Photothermal ionization spectrum of M.I.T.'s MBE-92.

as speculative. The line widths of all the peaks in both spectra are comparable and the relative peak amplitudes are for MBE-91: $Pb:X_1:(SeSn):Si::58.8:77.0:78.5:16.6$, and for MBE-92:$Pb:X_1:(SeSn):Si::69.5:33.0:43.2:33.4$.

The presence of Pb and X_1 in MBE-91 and MBE-92 turns attention once again to the abnormally broad peak labeled (SeSn) in the spectrum of MBE A-147. It is conceivable that the width of this peak may be due to the presence of unresolved Pb and/or X_1 peaks at lower energies, and in fact small shoulders on the (SeSn) peaks's low energy side can be seen at wavenumbers associated with these species but these are too small to be considered definitive.

In summary, all the MBE grown material has peaks associated with (SeSn) and Si. Both Pb and X_1 occur in the MIT samples and possibly in the Bell Labs sample, while C is present only in low concentration in the Bell Labs sample and absent entirely in the MIT samples.

MO-CVD SAMPLES

P.D. Dapkus of Rockwell International has provided us with three GaAs samples MO-CVD Seq. 29, Seq. 129, and Seq. 132 grown by the metal organic chemical vapor deposition (MO-CVD) growth technique. Photo-thermal ionization spectra for these samples appear in Figures 19, 20, and 21. In all three spectra, the dominant peak corresponds to that identified by Wolfe, Stillman and Korn[3] as C. That C should be incorporated into the MO-CVD grown material is not surprising in view of the organic carrier molecules present during growth. The dominance of this peak in all three spectra can be seen as a confirmation of the identification of C by Wolfe et al., as well as a determination of the primary residual donor species in MO-CVD material.
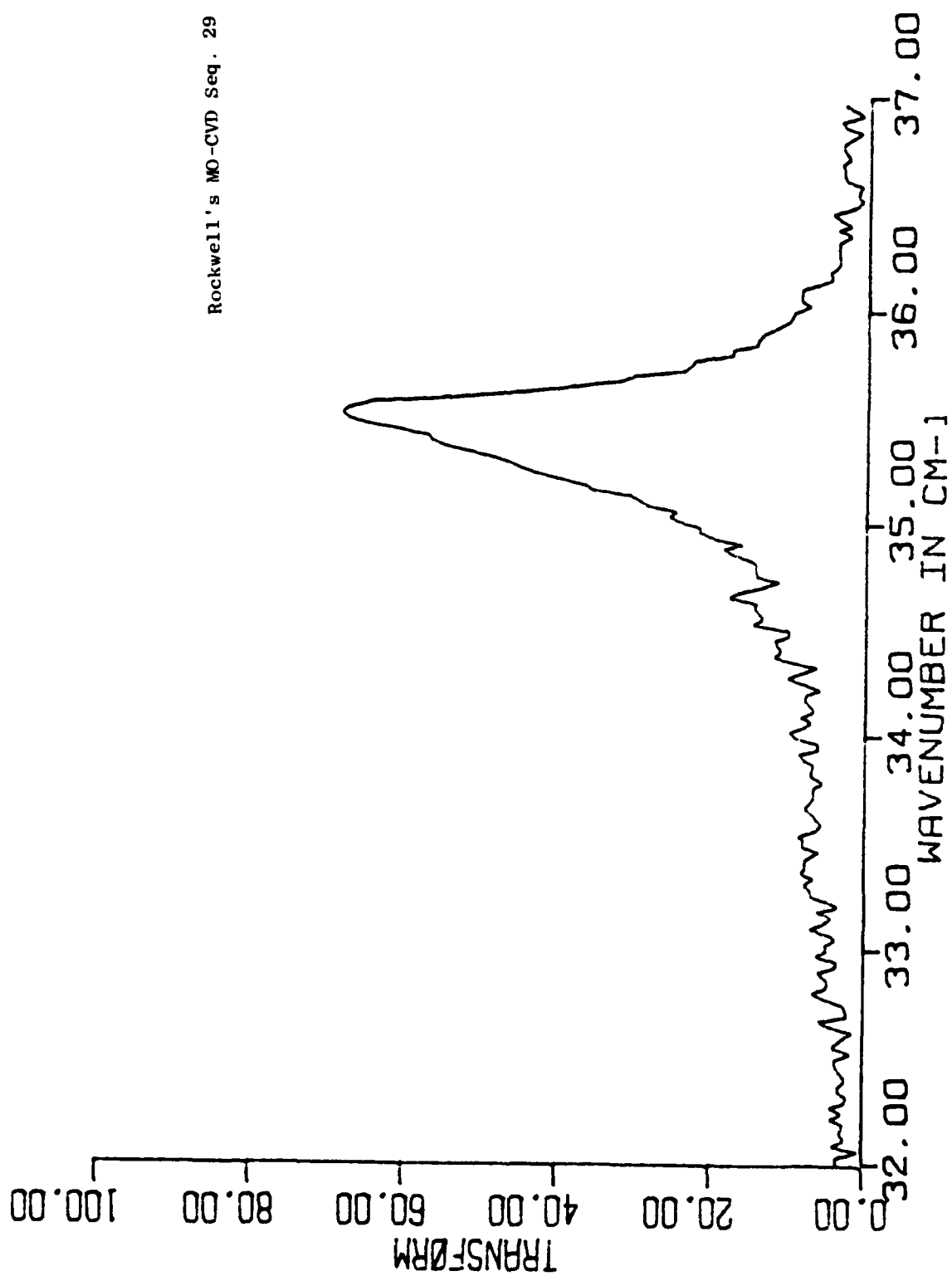
41

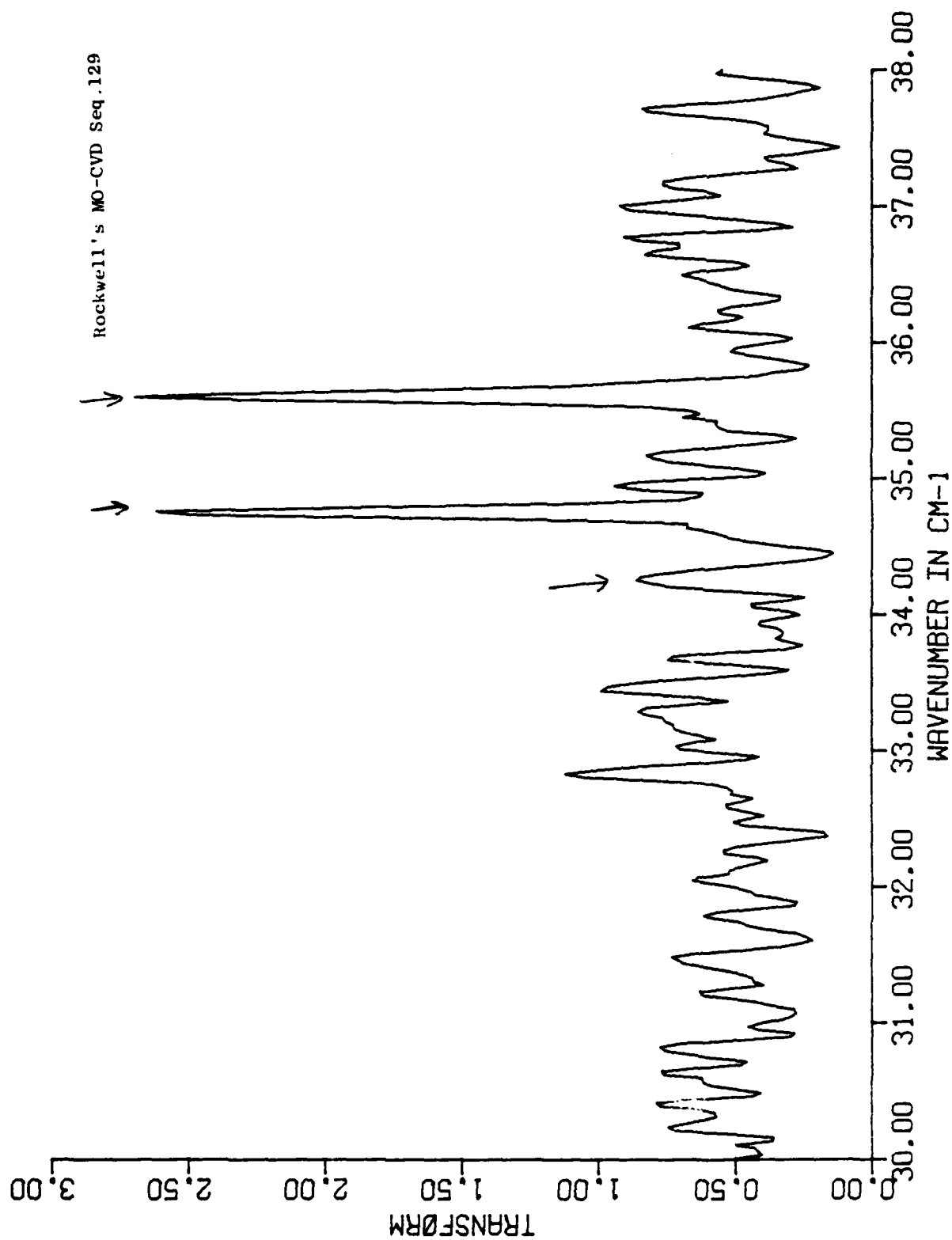Figure 19. Photothermal ionization spectrum of Rockwell's MO-CVD Seq. 29.

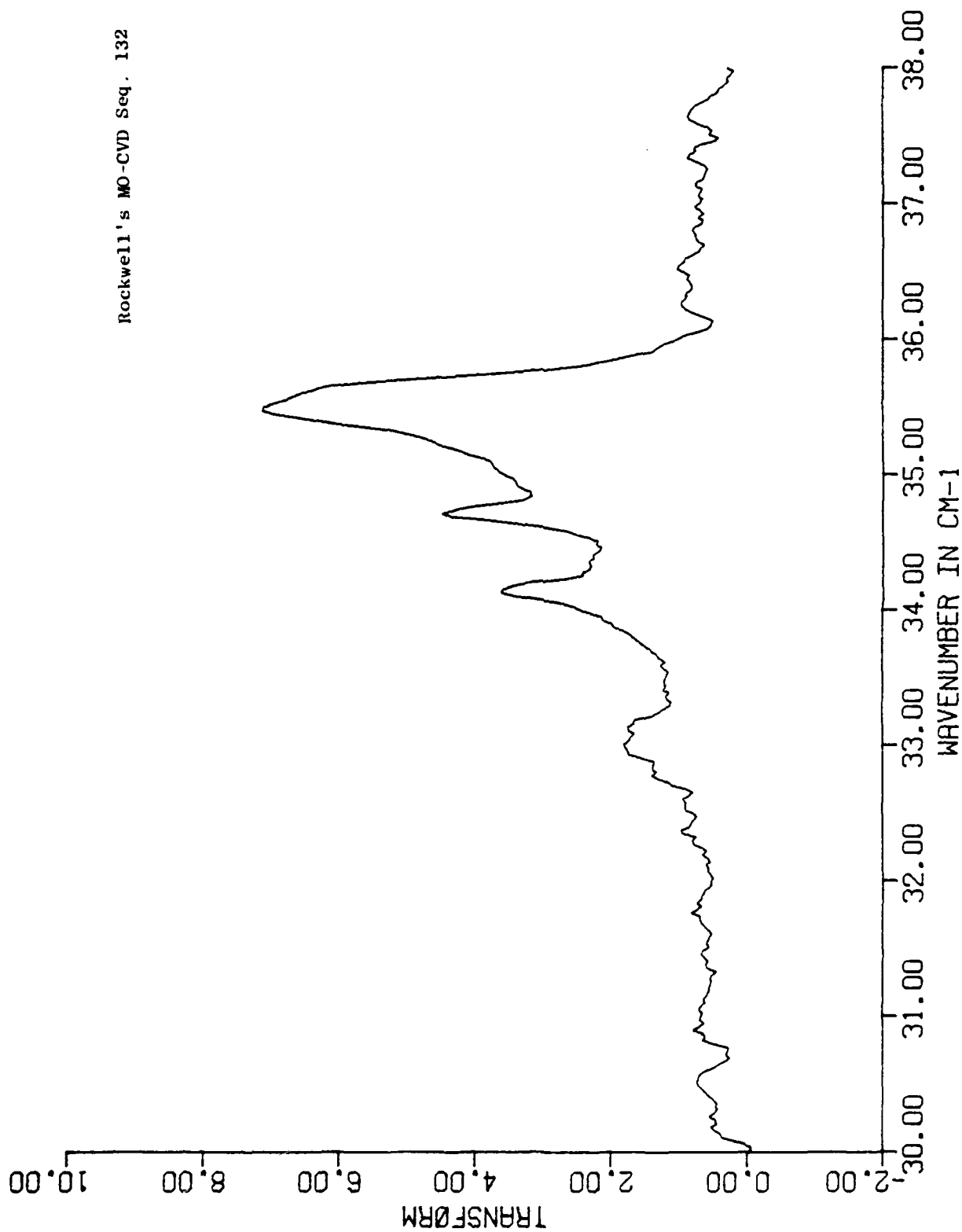Figure 20. Photothermal ionization spectrum of Rockwell's MO-CVD Seq. 129.

Figure 21. Photothermal ionization spectrum of Rockwell's MO-CVD Seq. 132.

It should be noted here that M.N. Asfar, K.S. Button, and G.L. McCoy, using neutron transmutation doping, have observed a peak at approximately the position (relative to the other peaks in the 1s-2p (m=-1) envelope) of the peak we have labeled as C. Asfar et al. have identified their peak as Ge in accordance with the expected capture of thermal neutrons by Ga nuclei in the GaAs lattice.

$$Ga + n \rightarrow e^- + Ge$$

$$As + n \rightarrow e^- + Se$$
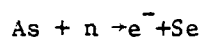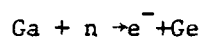
The corresponding neutron capture reaction by As results in transmutation to Se whose photothermal ionization peak position has been identified by C.M. Wolfe, G.E. Stillman, and D.M. Korn.[3] Asfar et al. also observed a peak at a position in agreement with this identification in their transmutation doped material.

In the text of their paper, Asfar et al. suggest that the position of the peak they identify with Ge should not be associated with C. There is no reason to suspect a priori that a peak position should be uniquely held by a single donor species. This is especially true in view of the large number of donor species and the narrow range of wavenumbers (compared to a peak line width) over which the 1s-2p (m=-1) transitions occur. Moreover, it is difficult to imagine how the dominant peak in the spectra of all of our MO-CVD samples could be attributed to Ge and not C. In addition, the Ge identification by Asfar et al. contradicts identifications by C. Wolfe, et al.,[3] R. Cooke et al.,[10] and M. Ozeki et al.[11] All three of these groups have identified a peak at lower wavenumber (about 0.6 cm^{-1} above the Si peak at 50 kilogauss) in Ge back doped samples. Perhaps Ge introduces more than one shallow donor level in GaAs. If C and Ge do, in fact, introduce peaks at or near the same

45

wavenumber within the 1s-2p (m=-1) envelope, this may hinder or even preclude discrimination between these donor species in GaAs.

In the spectrum of MO-CVD Seq. 29, a small peak at a wavenumber corresponding to Si is resolved, while in the spectra of Seq. 129 and Seq. 132 the Si peak has more than half the amplitude of the dominant C peak. Also in the spectrum of Seq. 132 (which was grown at 600°C) a large peak at the position of X_1 is seen, while in the spectrum of Seq. 129 (which was grown at 575°C under conditions otherwise identical to those of Seq. 132) the X_1 peak is absent. Because of the possible association of X_1 with a Ga vacancy-impurity complex, this may be an indication of increased vacancy formation at the higher growth temperature.

The relative peak amplitudes in these samples' spectra are Si:C:: 1.8:6.8 in Seq. 29, Si:C::6.0:1.04 (at 25 kilogauss) in Seq. 129, and X_1:Si:C::3.54:4.40:7.06 in Seq. 132.

VPE SAMPLES

Three samples grown by vapor phase epitaxi (VPE) were measured. The first of these B61-11 was grown by C.M. Wolfe, while he was at MIT Lincoln Laboratory using an $AsCl_3$ growth technique. The other two samples GaAs-763 and GaAs 775 were grown by J.K. Kennedy at Hanscom Air Force Base using the AsH_3 hydride technique. The spectra of all three samples have peaks due to X_1, Si, and C. (See Figs. 22, 23, and 24.)

The spectrum of B61-11 shows the extremely small line widths associated with such high purity and lightly compensated material. Donor and acceptor concentrations in this sample were determined from 77 K Hall measurements to be N_D=5.41x10^{13} cm^{-3} and N_A=9.44x10^{12} cm^{-3} with μ_{77}=200,993 cm^2/Vsec.
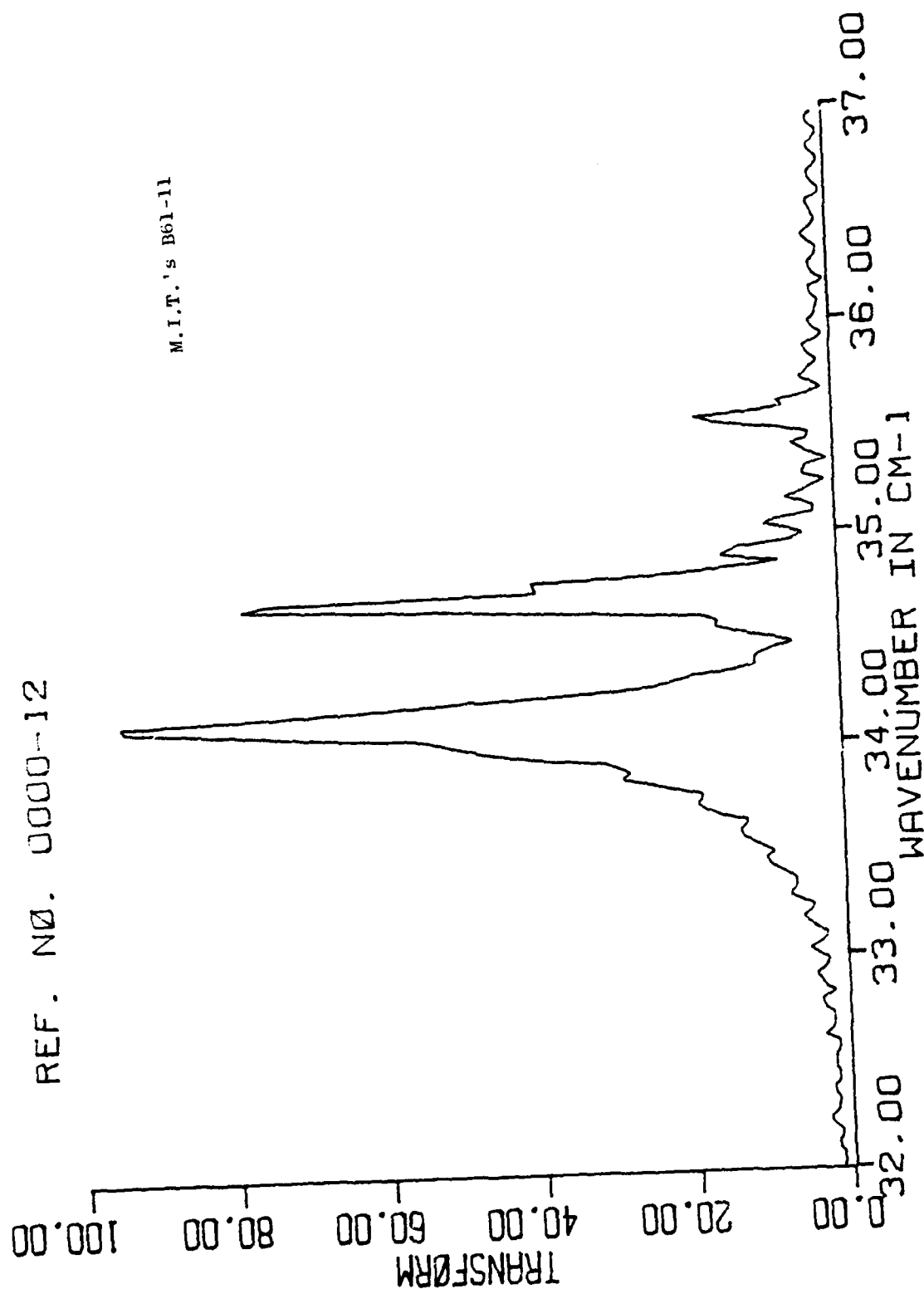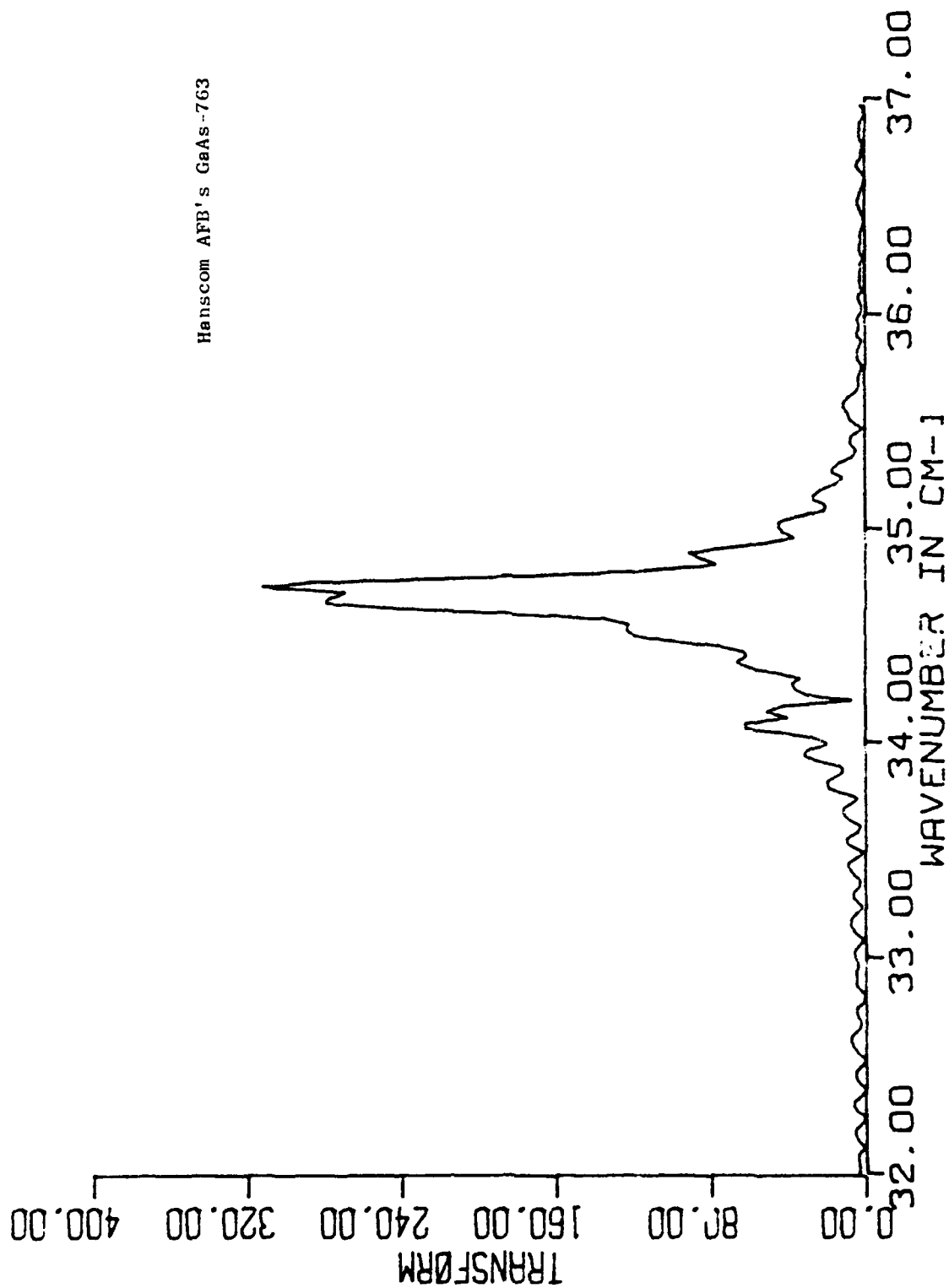
Figure 22. Photothermal ionization spectrum of M.I.T.'s B61-11.

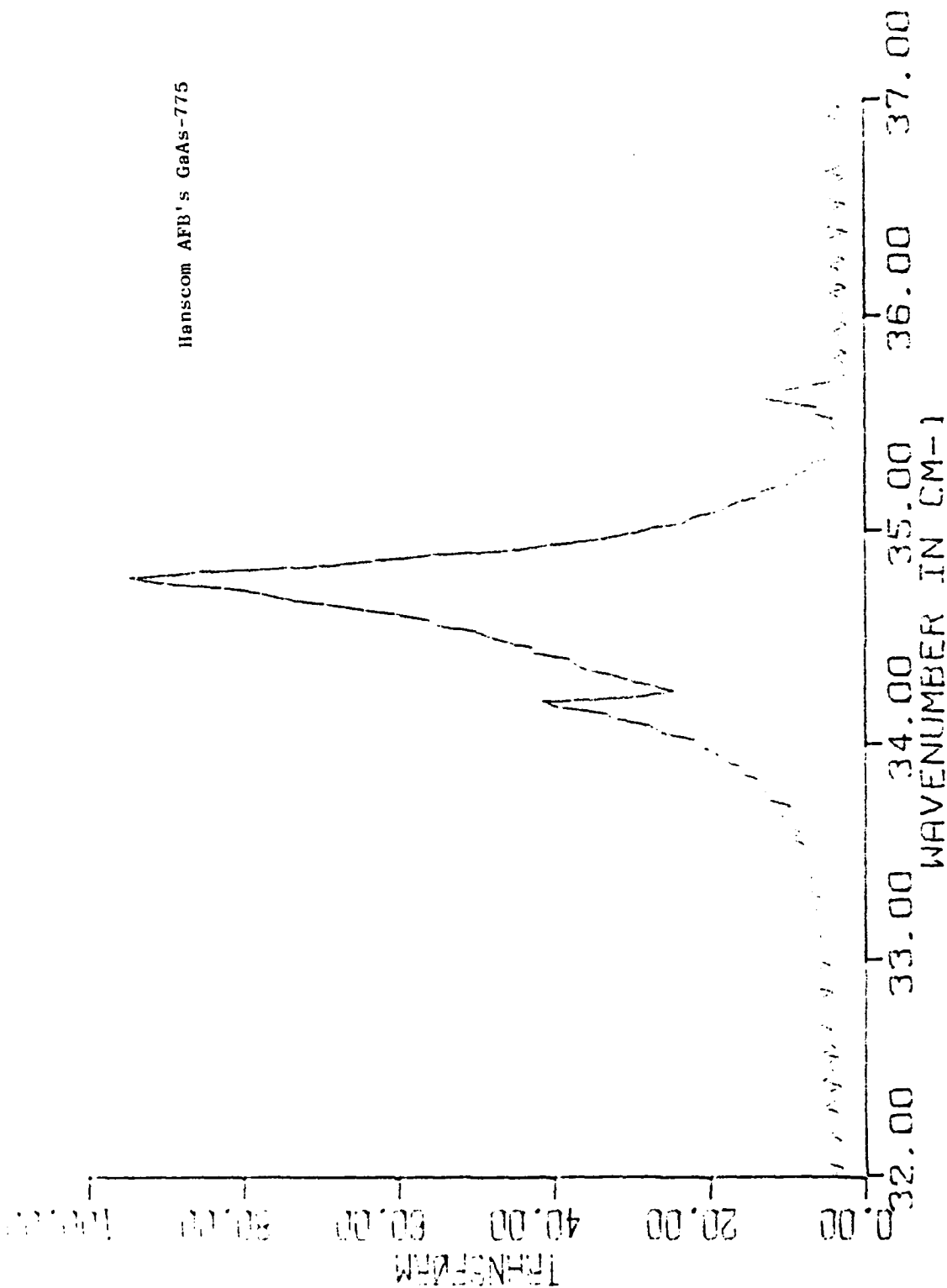Figure 23. Photothermal ionization spectrum of Hanscom AFB's GaAs-763.

Figure 24. Photothermal ionization spectrum of Hanscom AFB's GaAs-775.

This is the best quality GaAs sample we have measured, and because of the narrow peaks in its photoconductivity spectrum, it has been used as a standard for identifying peaks in the spectra of other samples. The oscillations seen in the spectra of B61-11 are mostly due to the convolution of the extremely narrow lines with the instrument function of the spectrometer. Alternatively, they can be thought of as Gibbs phenomenon resulting from the finite path length over which the interferogram must be measured. These oscillations decrease in wavelength and amplitude as the path length over which the interferogram is measured is increased.

The spectrum of B61-11 is typical of that of the best undoped samples grown in C.M. Wolfes' $AsCl_3$ system except that the relative amplitude of the X_1 peak is a bit larger and of the C peak is a bit smaller with respect to the Si peak than has been usually seen. The ratios of peak amplitudes in the spectrum of B61-11 are $X_1:Si:C::83.1:78.6:17.8$, while in eight other high purity undoped GaAs samples grown in this system, spectra taken by G.E. Stillman at MIT Lincoln Laboratory show average relative peak amplitudes of $X_1:Si:C::0.22:1.0:0.76$.

In the spectra of both the samples GaAs-763 and GaAs-775, only peaks due to X_1, Si and C are seen. The relative peak amplitudes in GaAs-763 are $X_1:Si:C::62.3:312:11.3$ and in GaAs-775 are $X_1:Si:C::41.6:94.3:13.5$. Notice that in both these spectra the Si peak dominated followed in amplitude by the X_1 and then the C peak. The peaks in the spectrum of GaAs-763 are considerably narrower than those of GaAs-775 as would be expected from the factor of two difference in acceptor concentration which would cause difference in intensity of random electric fields responsible for Stark broadening.

50

LPE SAMPLES

L.F. Eastman of Cornell University has provided us with two GaAs samples SM-25A and SM-30 grown by the liquid phase epitaxy (LPE) growth technique. Another sample LPE-251(2) grown by J. Abrokwa at Honeywell using this technique was also measured. Photothermal ionization spectra for these samples appear in Figures 25, 26 and 27.

For the spectra of both SM-25A and SM-30 peaks due to either Se or Sn, and to Si are observed with roughly equal amplitudes. As was the case in the two hydride VPE samples, the LPE sample SM-25A, having lower acceptor concentration, has less Stark broadening in the peaks of the photoconductivity spectrum. (See Table III for the values of N_A and line widths.)

The sample LPE-251(2) is interesting in that its spectrum shows only one donor species is present. The peak in this spectrum is that of Si, and although there is some structure on the low energy side of this peak at wavenumbers close to those associated with X_1 and (SeSn), such structure may well be noise in the spectrum. It would be surprising to find an X_1 peak because to our knowledge this has never been seen in LPE grown material. Another interesting aspect of this spectrum is the narrowness of the Si peak. This is incommensurate with the rather low mobility and high acceptor concentration deduced for this sample from our 77 K Hall measurement.
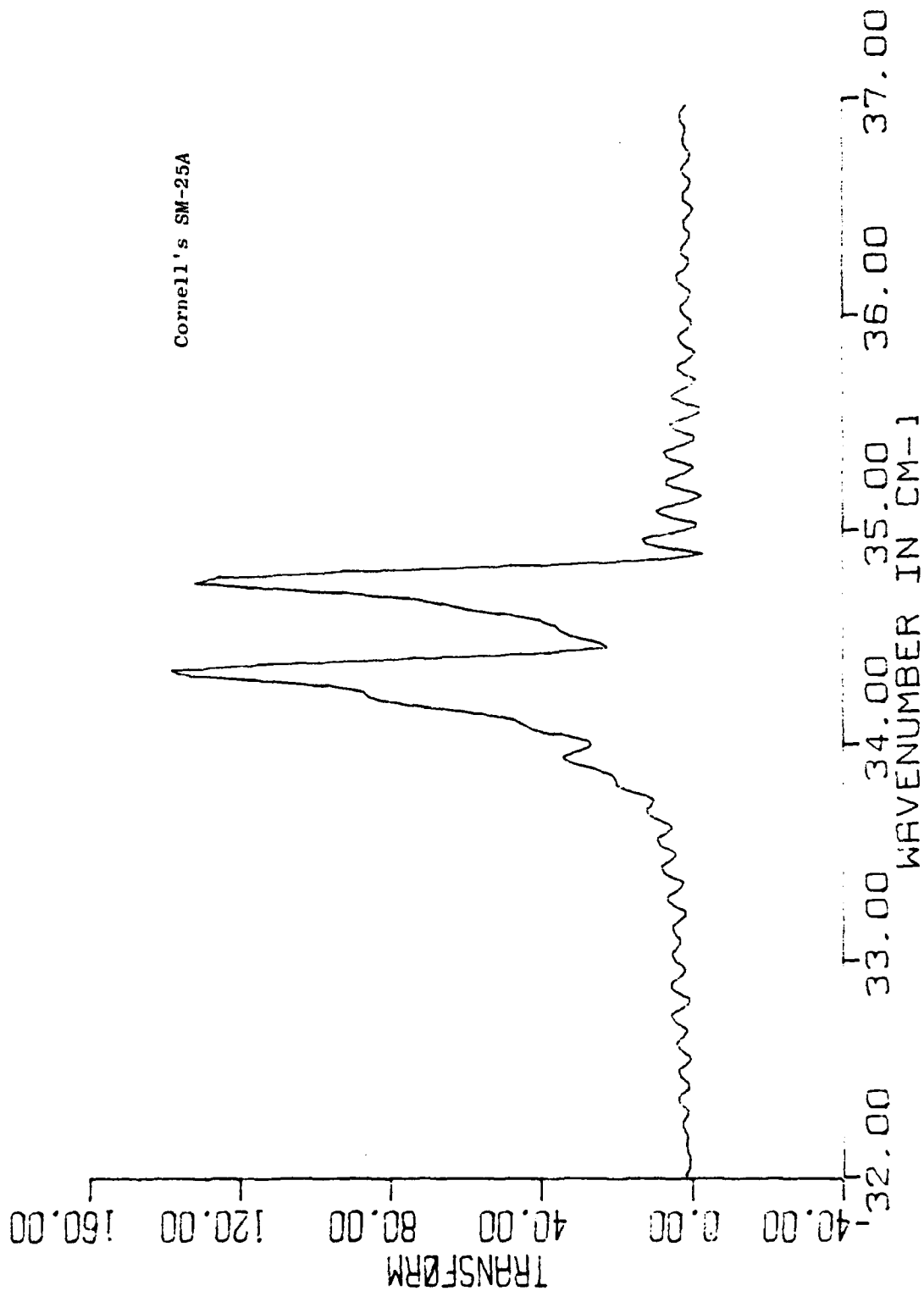
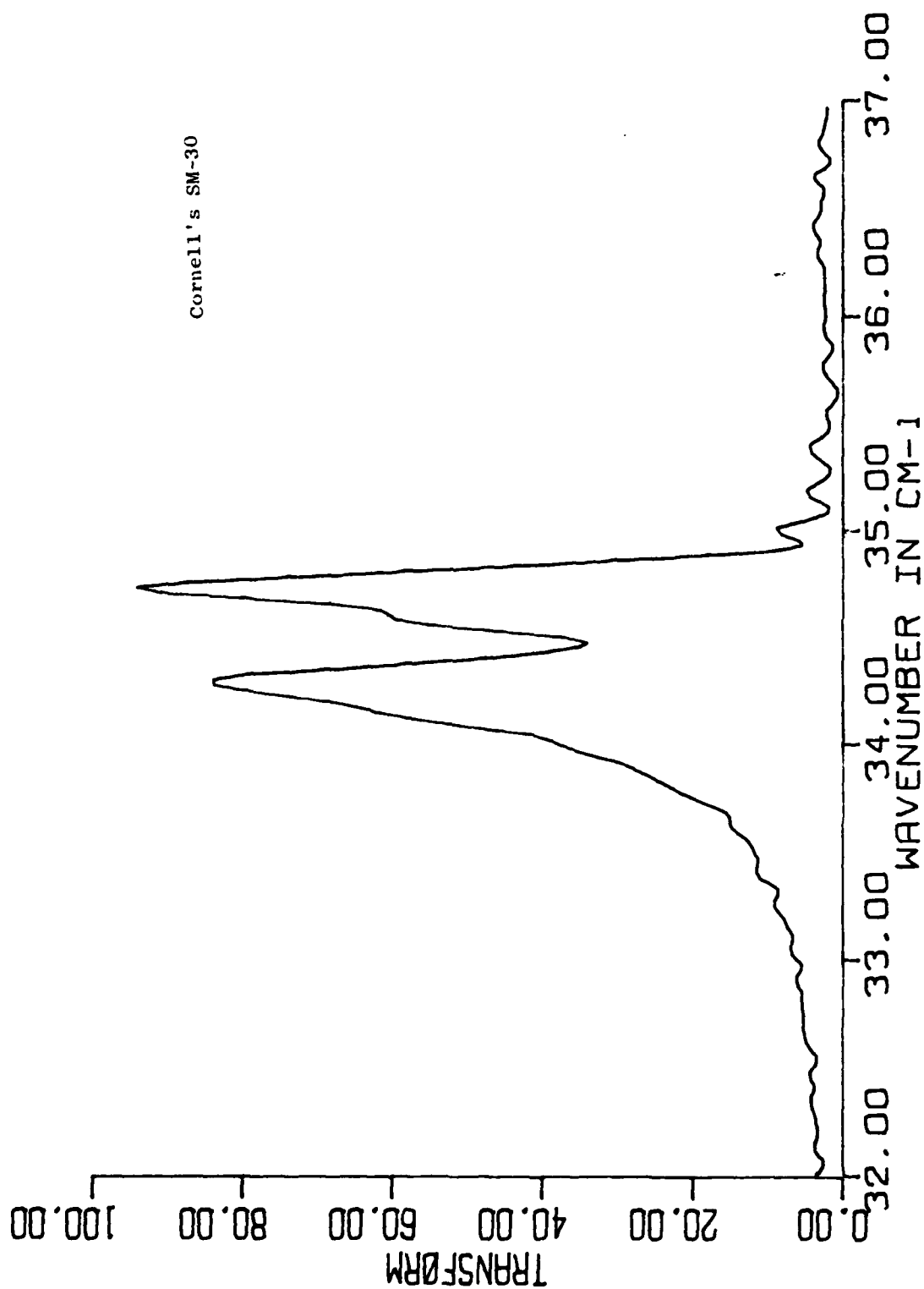Figure 25. Photothermal ionization spectrum of Cornell's SM-25A.

Cornell's SM-30

WAVENUMBER IN CM-1

TRANSFORM

Figure 26. Photothermal ionization spectrum of Cornell's SM-30.

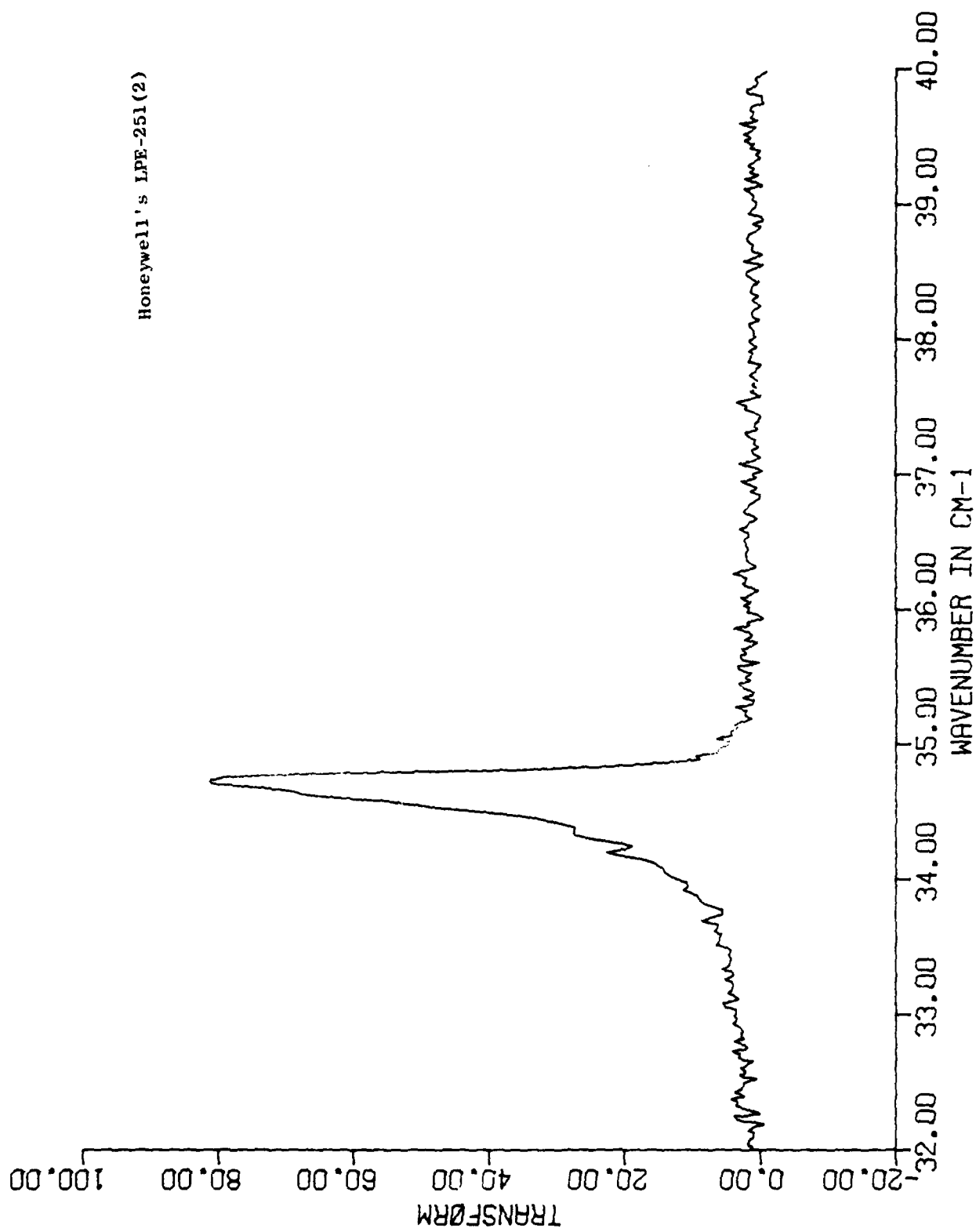Figure 27. Photothermal ionization spectrum of Honeywell's LPE-251(2).

Honeywell's LPE-251(2)

54

ACKNOWLEDGEMENTS

REFERENCES

1. W. Kohn, Shallow Impurity States in Silicon and Germanium in Seitz & Turnbull, Solid State Physics, Vol. 5, p. 257.

2. E.O. Kane, J. Phys. Chem. Solids, 1, 249 (1957).
   Q.W.F. Vrehen, J. Phys. Che. Solids 29, 129 (1968).

3. C.M. Wolfe, G.E. Stillman, D.M. Korn, Proc. 6th Int. Symp. GaAs (Inst. Phys. London 1976).

4. S.M. Kogan, T.M. Lifshits, Phys. Status Solidi (a) 39, 11 (1977).

5. E.E. Haller, W.L. Hansen, G.S. Hubbard, F.S. Goulding, IEEE Trans. Nucl. Sci. NS-23, 81, (1976).

6. G.E. Stillman, C.M. Wolfe, J.O. Dimmock, Far Infrared Photoconductivity in GaAs in Willards & Beer, Semiconductors and Semimetals, Vol. 12, Infrared Detectors (II), Ch. 4, p. 169.

7. D.M. Larsen, Phys. Rev. B, 8, #2, 535 (1973).

8. L. Mertz, Transformations in Optics, Wiley, New York, (1965).

9. M.N. Asfar, K.J. Button, G.L. McCoy, Int. J. of Infrared and Millimeter Waves, 1, No. 3 (1980).

10. R.A. Cooke, R.A. Hoult, R.F. Kirkman, R.A. Stradling, J. Phys. D, VII, (1978), p. 945.

11. M. Ozeki, K. Kitahara, K. Nakai, A. Shibatomi, K. Dazai, S. Okawa, O. Ryuzan, Jap. J. Appl. Phys. V16, No.9, 1617 (1977).

12. G.E. Stillman, C.M. Wolfe, D.M. Korn, Proc. 13th Int. Conf. on Phys. Semi., Rome, (1976), p. 623.

DISTRIBUTION LIST FOR CONTRACT :

Mr. Hunter Chilton
RADC/OCTE
Griffiss AFB, NY 13441

Dr. Y. S. Parks
AFAL/DHR
Wright-Patterson AFB, OH 45433

Mr. Lothar Wandinger
ECOM/AMSEL/TL/IJ
Fort Monmouth, NH 07703

Dr. George Gamota
Staff Specialist for Research
OUSDRE, Room 3D1067
Pentagon
Washington, DC 20301

Dr. Harry Wieder
Naval Ocean Systems Center
Code 922
271 Catalina Blvd.
San Diego, CA 92152

Dr. L. Sumney
Office of the Director of Defense
Research & Engineering
Washington, DC 20301

Dr. John Kennedy
RADC/ESM
Hanscom AFB, MA 01731

Dr. R. Reynolds
Advanced Research Project Agency
1400 Wilson Blvd.
Arlington, VA 22209

Dr. C. Sahagian
RADC/ETSP
Hanscom AFB, MA 01731

Dr. L. C. Kravitz
Director of Electronic & Solid State
Sciences (223)
Air Force Office of Scientific Research
Bldg. 410
Bolling Air Force Base
Washington, DC 20332

Mr. Don Reynolds
AFAL/DHR
Wright-Patterson AFB, OH 45433

Mr. Max Yoder
Office of Naval Research
Code 427
800 North Quincy St.
Arlington, VA 22217

Mr. Nathan Butler
Naval Electronic Systems Command
Washington, DC 20361

Dr. L. Cooper
Office of Naval Research
Code 427
800 North Quincy St.
Arlington, VA 22217

Mr. J. Cauffman
Naval Electronic Systems Command
Washington, DC 20360

Mr. J. W. Willis
Naval Air Systems Command
Washington, DC 20361

Dr. A. Glista
Naval Air Systems Command
Washington, DC 20361

Dr. J. Dimmock
Office of Naval Research
Code 427
800 North Quincy St.
Arlington, VA 22217

Dr. A. D. Klein
Naval Air Systems Command
Washington, DC 20361

Dr. H. J. Mueller
Naval Air Systems Command
Washington, DC 20361

Dr. Thomas AuCoin
USAECOM
DRSEL-TL-ESG
Fort Monmouth, NJ 07703

Dr. H. Whitman
U. S. Army Research Office
P. O. Box 12211
Research Triangle Park
Raleigh, NC 27709

Dr. H. R. Riedl
Naval Surface Weapon Center
Code WR-34
White Oak, Silver Spring, MD 20910

Dr. F. Barbe
Department of Navy
Office of ASNRES
Room 5E787
Pentagon
Washington, DC 20350

Dr. Robert Pohanka
Office of Naval Research
BCT#1 (619)
800 North Quincy St.
Arlington, VA 22217

Dr. E. Teppo
Naval Weapons Center
China Lake, CA 93555

Dr. Guenther H. Winkler
Code 381
Naval Weapons Center
China Lake, CA 93555

Mr. William Gutierrez
Night Vision & Electro Optics Lab.
Fort Belvoir, VA 22060

Dr. George Wright
Office of Naval Research
Code 427
Arlington, VA 22217

Dr. Fred Rothwarf
U. S. Army Electronic Technology &
Devices Lab. ERADCOM
Fort Monmouth, NJ 07703

Advisory Group on Electron Devices
201 Varick St.
New York, NY 10014

Defense Documentation Center
Cameron Station
Alexandria, VA 22314

Mr. M. Siegmann
Code 6804
Naval Research Laboratory
Washington, DC 20375

NRL: (Standard Distribution List)

Code 6800, 6802, 6803, 6810, 6820
      6850, 6870, 6890